Check for updates

A review on bismuth oxyhalide based materials for photocatalysis

Xuejiao Wei,[ab] Muhammad Usama Akbar,[c] Ali Raza [ID] *[c] and Gao Li [ID] *[b]

Photocatalytic solar energy transformation is the most encouraging solution to alleviate the environmental crisis and energy scarcity. Bismuth oxyhalide (BiOX) is an emerging class of materials that exhibits photocatalytic properties, such as resilient response to light, which causes enhanced energy conversion (solar energy) owing to their exceptional layered structure and attractive band structure. The present review presents a summary of results from the recent developments on the tuning and design of BiOX-based materials to improve the energy conversion. In particular, the preparation and tuning approaches that have the potential to enhance the photocatalytic behavior of BiOX and some other techniques, such as elemental doping, are addressed, which prevent the rapid recombination of charges, and formation of oxygen vacancies, facilitating an improvement in the photocatalytic reaction. Various frameworks are also presented, displaying the significance of BiOX-based nanocomposites. Finally, the main challenges and opportunities associated with the future progress of BiOX-based materials are presented. This review will provide an extended understanding and offer a preferred direction for the innovative design of BiOX-based materials for environmental and especially energy-based applications.

1. Introduction

Photocatalysis, which involves the successful use of solar energy, is a vital strategy for solving the energy crisis and environmental issues.[1–4] The inexhaustible energy from the sun can be utilized for the generation of hydrogen and carbon-containing fuels *via* water splitting and CO_2 photoreduction, respectively. Rational and novel photocatalyst designs are key factors for efficient photocatalytic activities.[5–9] Hydrogen is the most important source of energy considering a sustainable and clean future. The high combustion yield of H_2 energy generation (122 kJ mol^{-1}) makes it superior to the commonly used fuels such as gasoline and petroleum, and other fossil fuels.[4] Moreover, this method has the overwhelming advantage of environmental friendliness with no harmful and toxic by-products.[10,11] However, one drawback is the production of CO_2 during the process, which is extremely harmful to the environment.[12,13] Thus, the development of novel H_2 generation techniques is necessary to exclude the emission of harmful gases to the environment. Accordingly, one promising method to overcome this challenge involves the photocatalytic generation of H_2 in the presence of a catalyst under solar light irradiation, which is commonly referred to as "photocatalysis".[14–18]

Recently, a new class of photocatalysts comprising ternary (V–VI–VII) semiconductors such as bismuth oxyhalides (BiOX, X = Cl, Br and I) and metal-free catalysts including g-carbon nitride has emerged.[8,19–24] Specifically, slabs of [X–Bi–O–Bi–X] are combined *via* van der Waals forces to form a tetragonal matlockite crystal structure,[25–27] as depicted in Fig. 1. A deca-hedral asymmetric structure is formed when four oxygen atoms and four halogen atoms surround each central bismuth ion in [X–Bi–O–Bi–X]. The outstanding properties (optical, electronic, and structural) of these layered materials are generated from the synergistic effect of strong covalent bonding and van der Waals interaction among the atomic layers.[15]
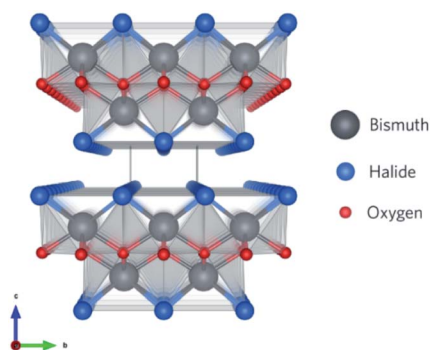
[a]*School of Chemical Engineering and Materials, Changzhou Institute of Technology, Changzhou 213032, China*

[b]*State Key Laboratory of Catalysis, Dalian Institute of Chemical Physics, Chinese Academy of Sciences, Dalian 116023, China. E-mail: gaoli@dicp.ac.cn*

[c]*Solar Cell Applications Research Lab, Department of Physics, Government College University Lahore, Punjab 54000, Pakistan. E-mail: ali.raza.physics@uskt.edu.pk*

Fig. 1 Framework of BiOX systems with stoichiometric X−Bi−O−Bi−X bilayers stacked along the *c*-axis. Reproduced with permission from ref. 28 Copyright 2016, the American Chemical Society.

In the past, BiOX materials were used as storage and ferroelectric materials, catalysts, and pigments. However, recently, they have found new applications in various fields including photocatalytic purification of wastewater and gases, oxidation of alcohols, water splitting, and organic synthesis.[29–32] Extensive works have been reported on the use of BiOX for the photocatalytic degradation of organic dyes in wastewater, but no significant studies have been reported on their PEC properties.[15,20,29,33,34] The high charge transfer ratio owing to their indirect band gaps together with their crystallinity makes these materials potential candidates for the production of H_2. Besides, enhanced charge separation can be obtained along the (001) plane of BiOX via an induced perpendicular internal electric field.[35] TiO_2 has been abundantly used for photocatalytic applications, but only shows activity in the UV (ultraviolet) region. In contrast, BiOX materials have the advantage of a wide bandgap range, varying from 3.3 eV (BiOCl) to 1.8 eV (BiOI), allowing visible light photocatalysis.[36,37] Since Zhang's group reported the fabrication of 3D-microspheres of BiOX on 2D-nanoplates via solvothermal synthesis for the degradation of methyl orange,[21] researchers have focused on the photocatalytic activity of BiOX materials.[38,39]

Similar to BiOX, $Bi_xO_yX_z$-based photocatalysts have a compact layered structure with weak interlayer interaction (nonbonding) and resilient interlayer bonding. A schematic illustration of the $Bi_4O_5Br_2$ crystal is presented in Fig. 2a as an example of the $Bi_xO_yX_z$-based structure. The layer structure of $Bi_4O_5Br_2$ comprises Bi–O layers that are positioned among double slabs of bromine ions. The Bi–O layers with respect to the surrounding charge density are greater compared to the dual bromine slabs of $Bi_4O_5Br_2$ (Fig. 2b).[40] The non-uniform

charge distribution among Bi–O layers and dual iodine slabs leads to polarization, resulting in a static internal electric field (IEF), which allows the splitting of excitons.[41,42] The growth route and IEF of layered $Bi_4O_5Br_2$ are in the [101] direction, which is altered to the [001] direction of BiOX. Experimental results and theoretical calculations (density functional theory (DFT) approach) have displayed the high photon absorption efficacy of $Bi_xO_yX_z$, which has also been investigated in earlier studies.[38,43] To enhance the activity of photocatalysts based on semiconductors, charge separation is considered an important factor. For $Bi_xO_yX_z$-based photocatalysts, the carrier separation efficacy primarily results from the IEF among their layers.[41] Usually, a higher value of IEF results in higher carrier separation efficiency for semiconductor photocatalysts. The electric field intensity is also based on the polarization force and space. The high dipole moment and interlayer spacing of $Bi_xO_yX_z$ result in an improved polarization force and space. Commonly, reducing the ratio of Bi to X results in a reduction in the optical absorption, which in turn reinforces the hybridization (for the conduction band to favor electron movement and support the splitting of photogenerated excitons).[42] Consequently, $Bi_xO_yX_z$ are outstanding photocatalytic materials.

To date, many BiOX nanostructures (e.g., nanowires, nanobelts, nanocrystals, nanosheets, nanofibers, hollow microspheres, porous nanospheres, and flower-like structures) have been fabricated.[26,44–47] However, a further improvement in the properties of BiOX is necessary for commercial applications, which is being attempted by boosting its photocatalytic potential via enhanced light absorption and photo-induced charge transfer efficiency. These improved BiOX photocatalysts show brilliant potential for wastewater treatment, H_2 generation, N_2 fixation, O_2 evolution, CO_2 reduction, disinfection, and organic synthesis.[15,48–54]

In the present review, we focus our discussion on the connection between the structural tailoring and enhancement of photocatalytic activity. This review is arranged as follows. Initially, we briefly discuss the synthesis protocols for BiOX, which is considered fundamental from an application point of view. Then, the photochemistry and schemes for solar energy harvesting such as hydrogen, oxygen production, and CO_2 reduction are also explored. Subsequently, we combine the most promising and evolving strategies for the enhancement of the photocatalytic activity of BiOX-based photocatalysts. We aim to establish a bridge between modern strategies and structural engineering toward better photocatalytic reactivity combined with maximum solar energy harvesting opportunities, which is the focal point of the present review. All these findings and summaries are supplemented with the addition of theoretical studies. Finally, we provide the current challenges and opportunities.

Fig. 2 Structure models of Bi_4O_5Br. (a) IEF direction and (b) charge density contour plots of the (101) surface. Reproduced with permission from ref. 40 Copyright 2016, Elsevier B.V.

2. Synthesis methods

2.1 Hydrolysis method

BiOCl can be prepared via the hydrolysis of different compounds including bismuth chlorides, nitrides, and oxides. Hydrolysis offers mild reaction conditions, but the products are
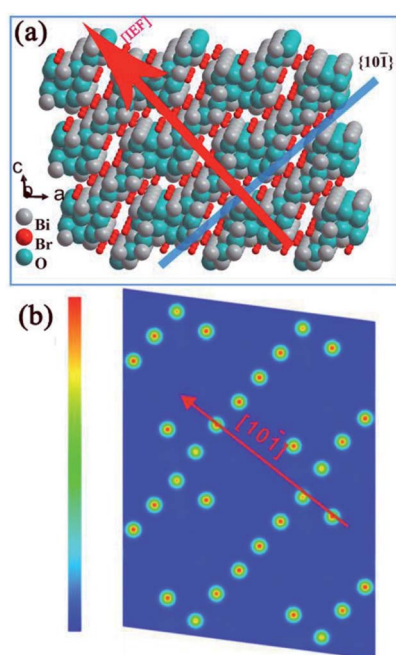
not dimensionally uniform. Armelao *et al.* synthesized BiOCl nanostructures *via* the hydrolysis of $BiCl_3$ for 6 h at 65 °C, which were stabilized using acetylacetone as an auxiliary solvent under an acidic environment.[55] Similarly, Song *et al.* reported that thick nanosheets (21 nm to 85 nm) of BiOCl could be synthesized *via* the hydrolysis of $Bi(NO_3)_3$ with HCl and Na_2CO_3 by maintaining the pH (~2) for 30 min at room temperature.[56]

2.2 Hydrothermal/solvothermal method

The hydrothermal method is the most common BiOCl preparation method, in which spontaneous pressure is produced to improve the reactivity and solubility of the precursors, causing chemical reactions to occur in the atmosphere.[57,58] The size, crystal structure, exposed surface, and shape of BiOCl can be easily controlled by changing the thermodynamics and kinetics. Gao *et al.* prepared BiOCl nanospheres by adding $Bi(NO_3)_3$ in ethylene glycol and NaCl solvent for 12 h at 160 °C.[59] Also, Liu *et al.* synthesized nanoplates by mixing $Bi(NO_3)_3$ in mannitol solution and NaCl was added to the resulting mixture.[60] The reaction was carried out for 3 h to form a suspension at more than 150 °C. The (001) plane at the four-sided surface and (110) plane at the top and bottom of the prepared sample were exposed. Ye *et al.*[61] fabricated $Bi_4O_5I_2$ and Bi_5O_7I *via* different treatments of the molecular precursors (Fig. 3).

2.3 Template method

A particular nano-sized material is used as a template, which enhances the growth in the template method. The symmetry (size and shape) of the prepared samples depends on the nature of the template used, which makes it a promising technique for the synthesis of BiOCl nanostructures. For instance, Cui *et al.* employed a template of carbonaceous microspheres and calcined Bi^{3+} with Cl^- (absorbed on template surface) from raw HCl and $Bi(NO_3)_3$ at a very high temperature of 400 °C to prepare hollow microspheres of BiOCl. The shell thickness and diameter of the uniform BiOCl microspheres were about 40 nm and 200 nm, respectively.[62] Yan *et al.* applied a biological template (butterfly wings) for the synthesis of hierarchical BiOCl.[63] It was found that the subsequent seed deposition of BiOCl and animation of the used template resulted in the formation of 2D BiOCl nanosheets uniformly raised on the template surface, replicating the complex and original fine structure of butterfly wings.

2.4 Calcination

Modified BiOX-based photocatalysts can be produced *via* heat treatment of pure BiOX materials. The phase transformation can easily be achieved because the unstable halogen atoms can escape easily owing to the weak van der Waals forces. For instance, Yu, *et al.* synthesized plate-like $Bi_{24}O_{31}Br_{10}$ through the heat treatment of BiOBr flakes at 750 °C and investigated its photocatalytic activity for the decomposition of Acid Orange II.[64] Besides, instead of the plate-like morphology, there various morphologies have also been observed. $Bi_{24}O_{31}Cl_{10}$ hollow microspheres were obtained *via* the thermal treatment (600 °C) of BiOCl in the presence of carbonaceous materials as sacrificial templates.[62] The mechanism occurring is shown in Fig. 4.

2.5 Molecular precursor method

Bismuth-rich $Bi_xO_yX_z$ photocatalysts are usually synthesized *via* the hydrothermal method under alkaline conditions. However, it has been found that a small change in pH leads to a phase transition in the product, and thus obtaining high purity single-phase samples is still challenging. Recently, Ye *et al.* reported the preparation of single-phase $Bi_4O_5X_2$ (X = Br and I) samples *via* the molecular precursor method, where $Bi_4O_5X_2$ was obtained by hydrolyzing the precursor.[40,65] Two main products, namely $Bi_4O_5Br_2$ microspheres (diameter: 1 μm) and $Bi_4O_5Br_2$ nanosheets (thickness: 1 μm) were obtained. Interestingly, the photocatalytic data shows that the bismuth-rich and thickness-ultrathin strategies play quite distinct roles in the reaction. The bismuth-rich strategy only increases the efficiency of CH_4 generation for the photoreduction of CO_2, whereas efficient CO generation is only associated with the thickness-ultrathin strategies.[40] Presently, hierarchical bismuth-rich $Bi_4O_5Br_xI_{2-x}$ can also be obtained *via* the molecular precursor method, and enhanced activity was found in the photocatalytic reaction of CO_2 conversion under visible light.[66] BiOCl with a nanosheet morphology can be acquired *via* the hydrolysis of $Bi_n(Tu)_xCl_{3n}$ (Tu = thiourea). Importantly, the percentage of {001} plane was
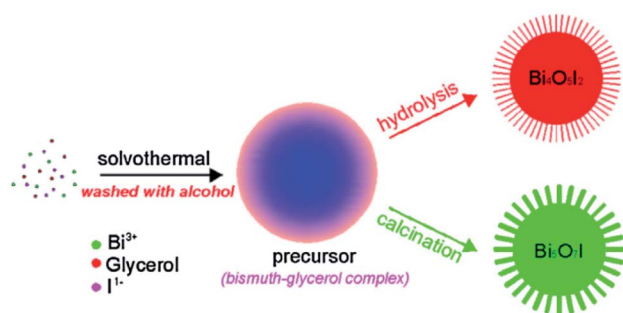

Fig. 3 Schematic illustration of the synthetic procedure for the preparation of $Bi_4O_5I_2$ and Bi_5O_7I *via* different methods. Reproduced with permission from ref. 61 Copyright 2016, Elsevier B.V.
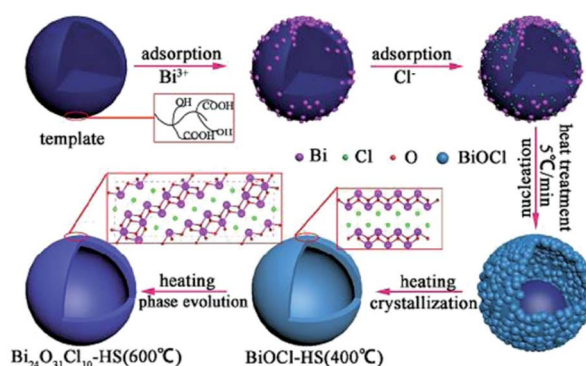

Fig. 4 Formation mechanism of bismuth oxychloride hollow microspheres. Reproduced with permission from ref. 62 Copyright 2016, Springer Nature.

determined by adjusting the $BiCl_3$: Tu feed ratio, and it was found that the percentage of {001} plane was positively proportional to the photoactivity of BiOCl.

3. Fundamentals of photocatalysis

3.1 H_2 evolution

The sun is the most remarkable energy source in nature because of its clean nature and diversity, though it is not easy to harvest, convert and store. Therefore, researchers have focused their attention on using sunshine and turning it into a green energy supply that is effective and readily available. The difficulties regarding the capture and storage of energy can be addressed by using hydrogen as an alternative clean energy source, which has many future applications such as stationary power generation, domestic heating, and environmental-friendly vehicles with zero pollution. The energy shortage problem can be resolved if we can use scattered sunlight for hydrogen generation via electrochemical, photochemical, and photoelectrochemical methods. Several limited methods have been used for the conversion of solar energy, but the production of hydrogen by water splitting using sunlight has attracted more interest due to its many advantages as follows.[67–72] (i) This process is based on clean water, which is a source of energy together with photon energy. (ii) It produces no pollutants and by-products (environmentally friendly). (iii) Hydrogen production via photochemical reaction efficiently deals with solar influx seasonal variation.[73]

Two main processes are involved in hydrogen generation via photocatalysis, i.e., photo-physical (PP) and electrochemical (EC) (see Fig. 5). In the photophysical process, the absorption of photons by electrons present in the valence band (VB) produces electron–hole pairs and transports electrons to the reaction sites at the conduction band (CB). In contrast, the

photochemical process defines water splitting by redox reactions. Generally, a photocatalyst absorbs only photons whose energy corresponds to its bandgap energy. A photon with the same or greater energy than the bandgap energy of the photocatalyst will have enough potential to eject an electron from the VB of the photocatalyst to its CB (leaving holes behind). Photon absorption results in the creation of excited electrons and holes, while the electrons in the CB may recombine with holes radiatively/nonradiative. This is an inevitable process regardless of the semiconductor used for photocatalysis.[4,75–77] The recombination rate is a vital element for low quantum efficiency for any photocatalyst.[75,78–80] The photo-excited carriers that survive recombination then migrate to the surface of the photocatalyst, where photocatalytic reactions (hydrogen evolution reaction (HER) and oxygen evolution reaction (OER)) occur via diffusion/electric fields, which are related to the electrolyte or semiconductor interfaces.[81,82]

The generation of excitons is typically limited below 100 fs (femtosecond) and the average lifetime of excitons is around a few hundred ps (picoseconds). The diffusion of an electron lasts for a few ps, while the corresponding time for the transition of holes, at most, may be less than 100–300 fs.[75,83] Trap sites in semiconductors also play a role in restricting the recombination of photo-excited carriers. The greater the number of trap sites present in a catalyst (semiconductor), the lower the diffusion coefficients of electron/holes.[84,85] The trapping of electrons has a shorter lifetime (a few microseconds) than holes, whose trapping, recombination, and surface transfer processes occur significantly faster (in pico- and nano-second range).

3.2 O_2 evolution

The photocatalytic production of O_2 is considered the rate-determining phase for splitting water to produce H_2. Compared to the transformation process, which involves two electrons from H^+ to H_2, the production of O_2 requires four holes to participate in the oxidation of OH^- and H_2O to obtain O_2 to overcome the large kinetic barrier. Thus, it is necessary to boost the water splitting oxidation half-reaction for the more efficient generation of H_2. Previously, studies have been reported on the O_2 production capability of BiOBr and BiOCl.[87,88] For the currently established $Bi_xO_yX_z$ materials, improved activity for the production of O_2 can be achieved. Lin et al.[89] established a heterostructure of $Bi_3O_4Cl/BiOCl$ and employed it via a Z-scheme for O_2 production. $Bi_3O_4Cl/BiOCl$ exhibited a formation rate 58.6 $\mu mol\ g^{-1}\ h^{-1}\ O_2$ with $FeCl_3$ and $AgNO_3$ as electron scavengers. They established that the oxygen vacancy adjusted the $Bi_7O_9I_3$ flowered microspheres through the ionic liquid-assisted method.[90] These $Bi_7O_9I_3$ microspheres with excessive oxygen could deliver O_2 with a generation rate of 199.26 $\mu mol\ g^{-1}\ h^{-1}$ with $AgNO_3$ as an electron sacrificial agent. Hu et al.[91] used polyvinylpyrrolidone (PVP) and cetyltrimethylammonium bromide (CTAB) to tune the morphology of Bi_3O_4Br to nanorings. Due to the ring structures, appropriate band potentials, and exposure of the (001) plane, the improved adsorption/migration of carriers and mass could be achieved over the nanorings of Bi_3O_4Br. Therefore, the Bi_3O_4Br nanorings
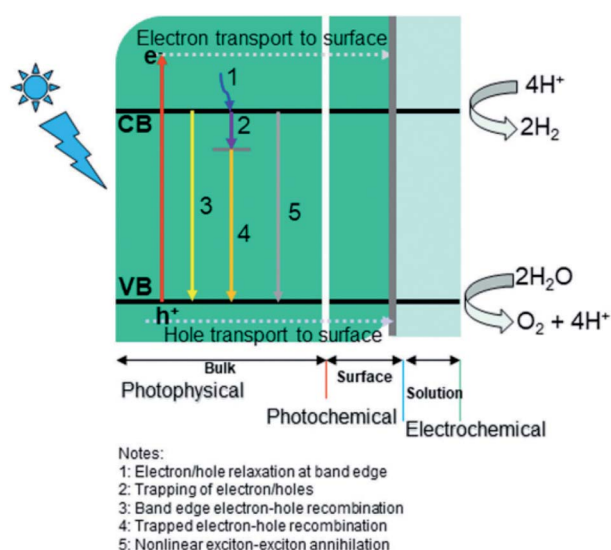

Fig. 5 Key dynamic processes involved in water–splitting: (i) photophysical, (ii) photochemical, and (iii) electrochemical. Reproduced with permission from ref. 74 Copyright 2019, the American Chemical Society.
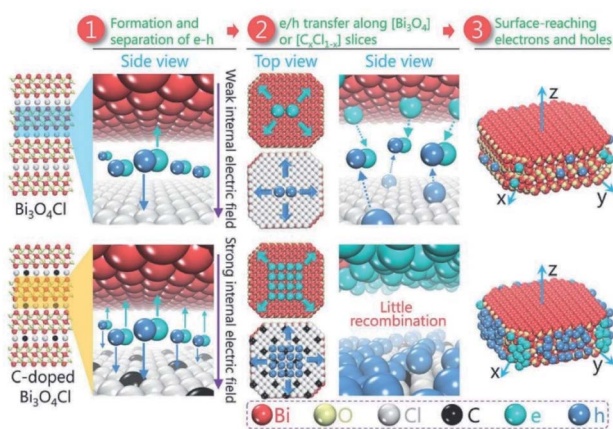
Fig. 6 Schematic design of the separation and the migration of holes and electrons in the bulk of pure and C-doped Bi_3O_4Cl. Reproduced with permission from ref. 86 Copyright 2016, Wiley-VCH.

delivered a production rate of 725.4 $\mu mol\ g^{-1}\ h^{-1}\ O_2$ with $Fe(NO_3)_3$ as an electron capture agent under sunlight.

Besides surface defect engineering and morphological control, Li *et al.*[86] employed C doping to boost the intrinsic electrical field in Bi_3O_4Cl (Fig. 6). Due to the substitution of Cl atoms in the crystal lattice by C doping, the electrostatic potential between [Cl] and $[Bi_3O_4]$ could be enhanced up to 7.36. Thus, the internal electrical field in Bi_3O_4Cl can be maximized, which can considerably reduce the possibility of carrier recombination. Upon irradiation, photo-generated electrons will transfer along the $[Bi_3O_4]$ layer to the [010] plane and holes will transfer along the $[C_xCl_{1-x}]$ layer to the [110] plane, as verified by the photo-deposition experiment and calculated density of states (DOS). Due to these features, $C–Bi_3O_4Cl$ delivered a production rate of $\sim$860 $\mu mol\ g^{-1}\ h^{-1}\ O_2$ under sunlight irradiation. This O_2 production rate could be maintained for up to 73 h in the cycle experiment.

3.3 CO_2 reduction

In the last two decades, photocatalytic activity has been considered a green method for converting CO_2 into useful hydrocarbon fuels and eradicating the greenhouse effect.[92–94] In comparison with water splitting ability to obtain H_2, $Bi_xO_yX_z$ displays encouraging potential in the photoreduction of CO_2 into solar fuel (CH_3OH, CH_4, CO, *etc.*). $Bi_xO_yX_z$ exhibits an enhanced photocatalytic reduction performance compared to BiOX due to its lower CBM potential. For example, $Bi_4O_5Br_2$ microspheres were synthesized and used for the photoreduction of CO_2. It was demonstrated that $Bi_4O_5Br_2$ could effectively photoreduce CO_2 under sunlight because based on the bismuth-rich and thickness-ultrathin strategies.[40] As illustrated in Fig. 7, the generation of CH_4 and CO by $Bi_4O_5Br_2$ was 2.04 and 2.73 $\mu mol\ g^{-1}\ h^{-1}$, which was higher than that by ultrathin BiOBr (CH_4: 0.16 $\mu mol\ g^{-1}\ h^{-1}$: CO: 2.67 $\mu mol\ g^{-1}\ h^{-1}$) and bulk BiOBr (CH_4: $\mu mol\ g^{-1}\ h^{-1}$; CO: 1.68 $\mu mol\ g^{-1}\ h^{-1}$), respectively. Moreover, it was also perceived that the bismuth-rich approach and the thick-ultrathin strategy induced the selective generation of CH_4 and CO, respectively. The apparent quantum yield
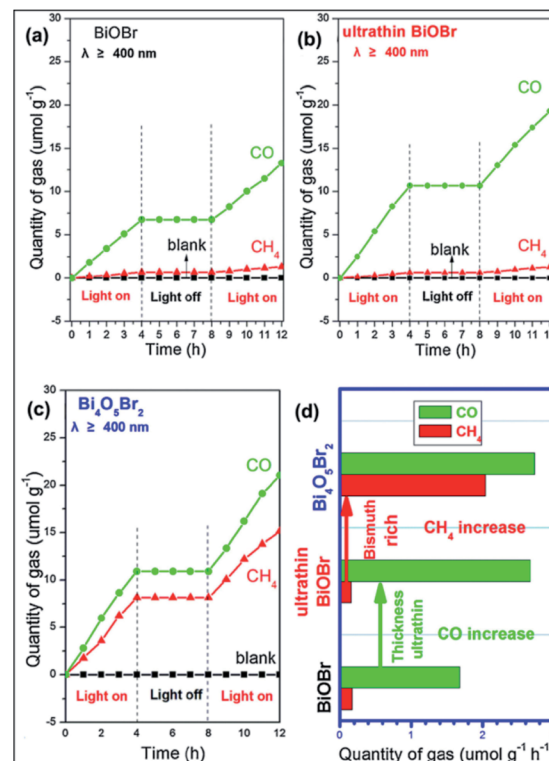

Fig. 7 Photocatalytic reduction performance for the conversion of CO_2 on (a) BiOBr; (b) ultrathin BiOBr; and (c) $Bi_4O_5Br_2$ and (d) comparison of solar fuel generation. Reproduced with permission from ref. 40 Copyright 2016, Elsevier B.V.

(AQY) for the photoreduction CO_2 into solar fuels at different wavelengths was calculated based on the following equation:[22]

$$AQY\ (\%) = \frac{N_{solar}}{N_p} = \frac{No.\ of\ reacted\ electrons}{No.\ of\ incident\ photons} \times 100\%$$

$Bi_4O_5I_2$, Bi_4O_5BrI, $Bi_4O_5Br_2$, and Bi_5O_7I have been developed for the photoreduction of CO_2 into CH_4 and CO upon exposure to sunlight. The AQY for solar fuels (CO and CH_4) manufactured by $Bi_4O_5I_2$ approached a maximum of 0.37% at the wavelength of 420 nm under monochromatic light irradiation.

3.4 N_2 fixation

The photocatalytic fixation of N_2 is very complex compared to other applications given that the photocatalytic reduction of N_2 to NH_3 is severely impaired by the weak nitrogen binding force on the surface of catalytic materials and the intermediate-high energy levels involved in the reaction.[38] Thus, to resolve this problem, efficient interface charge transfer from the catalyst to N_2 requires catalysts having strong electron donor ability and excess catalytic activation centers. The development of BiOBr nanosheets with oxygen vacancies on (001) facets is a typical example, which can fix N_2 to NH_3 upon exposure to visible light (Fig. 8).[50,95] For the manufacture of fertilizers and chemicals, the synthesis of ammonia (NH_3) is very important in agriculture and industry. The Haber–Bosch approach dominates commercial ammonia synthesis, which involves stringent reaction conditions
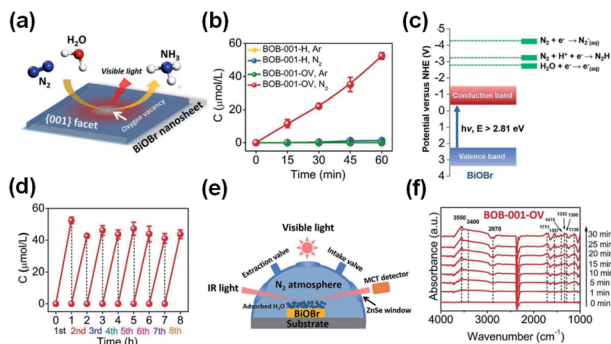
Fig. 8 (a) Scheme of N_2 fixation with water over BiOBr nanosheets. (b) Quantitative measurement of NH_3 generated under visible light ($\lambda >$ 420 nm). (c) Energy-level diagram and (d) Multi-cycle N_2 fixation on BOB-001-OV. (e) Reaction cell for the *in situ* IR signal measurement. (f) *In situ* IR signals of the photocatalytic N_2 fixation over BOB-001-OV. Reprinted with permission from ref. 50 Copyright 2015, the American Chemical Society.

(over 300 °C and 100 atm).[96] Thus, low-cost approaches for synthesizing artificial NH_3 need to be investigated under ambient conditions, among which, the sustainable reduction of photocatalytic N_2 is an excellent solution. A series of N_2 reduction experiments, particularly for bismuth-rich bismuth oxyhalides, was carried by Zhang's group,[50,97] demonstrating that BiOBr has suitable properties for the photoreduction of N_2 to yield ammonia. Ye *et al.*[98] reported that the N_2 photoreduction efficiency of Bi_5O_7I is facet dependent. Nanosheets of Bi_5O_7I with exposed (001) facets showed 2.3 times enhanced activity (111.5 *vs.* 47.6 μmol L^{-1} h^{-1}). However, Bi_5O_7I with exposed (100) facets displayed a higher NO_3-generation average than Bi_5O_7I with exposed (001) facets. It is important to note that 20% CH_3OH was used in this method as a sacrificial reagent.

For N_2 photoreduction in distilled water, researchers used defect-rich atomic-layer Bi_3O_4Br to prevent the use of a sacrificial reagent (Fig. 9).[99] The charges generated in the bulk will diffuse easily to the surface, benefiting from the single-unit-cell thickness. To facilitate surface-charge separation, surface defects also act as a center of charge separation (see Fig. 9a and b). In addition, the defective structure allows improved adsorption and N_2 activity (Fig. 9c), as shown by the reduction in adsorption energy on the perfect Bi_3O_4Br surface from -0.087 eV to -0.241 eV on a surface having defects. Consequently, the NH_3 formation rate if 50.8 μmol g^{-1} h^{-1} in water could be produced on a defect-rich Bi_3O_4Br layer between 9.2 and 30.9 times higher than the Bi_3O_4Br atomic layer (defect deficient) and bulk Bi_3O_4Br. In addition to the chemisorbed mode N_2 and N–H bending (Fig. 9e), the adsorption, activation and conversion of N_2 into NH_3 were further confirmed *via in situ* FTIR (Fig. 9d).

In 2021, Tiana *et al.*[100] prepared 1T phase WS_2 nanosheet (NS)-decorated Bi_5O_7Br NSs (1T-WS_2@Bi_5O_7Br) have a narrow band gap, effective carrier transport efficiency and good light absorption ability. After testing, the 1T-WS_2@Bi_5O_7Br-5 composite presented the best photocatalytic nitrogen fixation performance (8.43 mmol L^{-1} h^{-1} g^{-1}) and excellent stability. The probable photocatalytic mechanism of the 1T-WS_2@Bi_5-O_7Br composites was proposed. The Bi_5O_7Br NSs were prepared
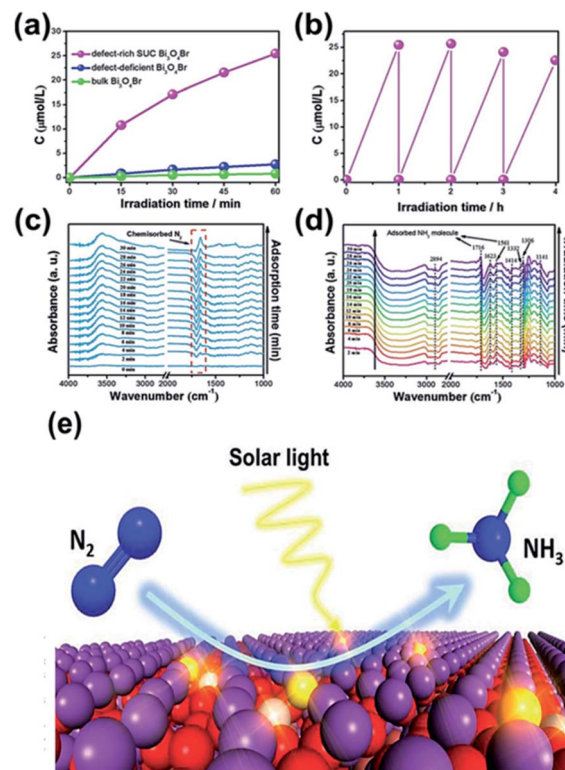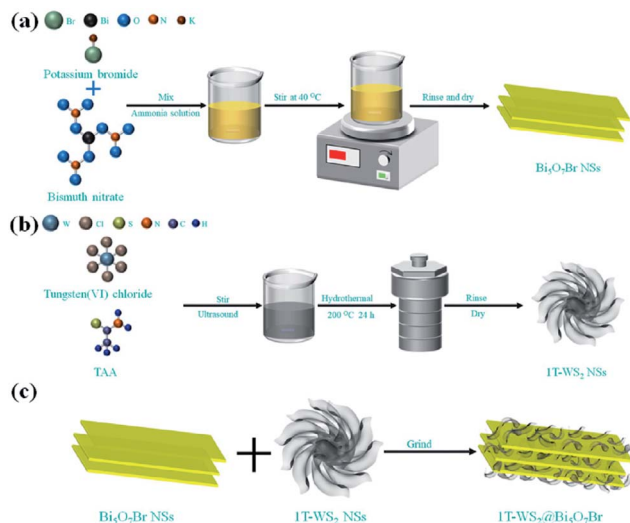

Fig. 9 (a) Quantitative evaluation of NH_3 generated and (b) stability of defect-rich SUC Bi_3O_4Br under light irradiation. *In situ* FTIR spectra of SUC Bi_3O_4Br catalysts during N_2 adsorption without irradiation (c) and under irradiation (d). (e) Scheme of the photocatalytic N_2 fixation process. Reprinted with permission from ref. 99 Copyright 2019 Wiley-VCH.

via a self-assembly water-induced process (Scheme 1a). Firstly, ammonia solution and bismuth(III) nitrate pentahydrate were added to a beaker, and then potassium bromide was added. Finally, the mixture was heated at 40 °C to obtain Bi_5O_7Br NSs with rich oxygen vacancies. As shown in Scheme 1b, the metallic 1T-WS_2 NSs were prepared *via* a solvothermal process. Tungsten(VI) chloride and TAA were dissolved in dimethylformamide (DMF), and then the mixed solution was hydrothermally heated at 200 °C for 24 h to obtain 1T-WS_2 NSs. The 1T-WS_2@Bi_5O_7Br composites were synthesized *via* an ordinary grinding process (Scheme 1c). The Bi_5O_7Br NSs and 1T-WS_2 NSs were added to a mortar with ethanol and hexane to fully grind. The mixed powder was dried to obtain 1T-WS_2@Bi_5O_7Br composites.

3.5 Pollutant removal

Pollutant removal is the most widely active photocatalytic application of $Bi_xO_yX_z$. Upon irradiation, electron and hole pairs can be generated in $Bi_xO_yX_z$, yielding various oxygen reactive species, such as singlet oxygen, $^\cdot O_2^-$, and $^\cdot OH$. By virtue of direct hole oxidation or reactive oxygen, different types of pollutants can be effectively removed, such as 4-*tert*-butylphenol, Rhodamine B (RhB), bisphenol-A (BPA), sodium pentachlorophenate, phenol, ciprofloxacin (CIP), resorcinol, acetaldehyde, tetracycline hydrochloride (TC), NO, and resorcinol.[102–109] Using the Bi-rich technique of $Bi_4O_5Br_2$ for

Scheme 1 Schematic route for the synthesis of (a) pure Bi$_5$O$_7$Br NSs, (b) 1T-WS$_2$ NSs and (c) 1T-WS$_2$@Bi$_5$O$_7$Br composites. Reprinted with permission from ref. 101 Copyright 2015, the American Chemical Society.

upshifting the CB edge, more active oxygen species could be produced over Bi$_4$O$_5$Br$_2$ relative to BiOBr. Consequently, 75% CIP was degraded by Bi$_4$O$_5$Br$_2$ after 120 min and 53.3% was mineralized after 180 min. In another report, our group synthesized Bi$_4$O$_5$I$_2$ and Bi$_4$O$_5$I$_2$ hollow nanotubes through a PVP-supported solvothermal process.[110] In comparison with Bi$_4$O$_5$I$_2$ nanosheets, the Bi$_4$O$_5$I$_2$ hollow nanotubes displayed an enhanced photocatalytic performance towards the degradation of BPA and RhB. The enhanced activity can be attributed to the confined highly concentrated active species induced by the tubular structure and the excellent electric conductivity. Xiao et al. prepared hierarchical microsheets of Bi$_7$O$_9$I$_3$ via a microwave-assisted method, which were employed for the photodegradation of BPA.[111] According to the complete organic carbon measurement, 89.1% BPA was eliminated by the Bi$_7$O$_9$I$_3$ microsheets almost after 1 h of irradiation, indicating that Bi$_7$O$_9$I$_3$ degrades BPA effectively. Conversely, the BPA degradation intermediates were measured by LC-MS chromatography. Besides water body pollutants, gas pollutants such as acetaldehyde and NO could be effectively removed by Bi$_x$O$_y$X$_z$.[105,112] For instance, Dong et al.[108] revealed that Bi$_4$O$_5$Br$_2$ nanosheets exhibited stable and high activity for the removal of NO. The NO removal efficiency over Bi$_4$O$_5$Br$_2$ reached 41.8% after 30 min irradiation and ·OH was found to be the main active species.

3.6 Organic syntheses

Currently, BiOX-based photocatalysts show potential under mild conditions for selective organic synthesis.[113] For example, surface-chlorinated BiOBr/TiO$_2$ transformed alkanes into an oxygenated product via the activation of C–H bonds under sunlight irradiation.[114] During the reaction, BiOBr with a narrow bandgap is excited, generating electron–hole pairs, and holes are transferred to the VB of TiO$_2$ which results in a positive VB position for TiO$_2$. The chlorine groups, which are

chemisorbed on the catalyst surface, trap the holes, producing chlorine radicals, and then control the activation of the C–H bond. In a recent report, ultrathin sheets of BiOCl were synthesized with hydrophobic properties, which was assisted by the in situ formation of water in an octadecylene solution via the reaction between oleic acid and oleylamine.[48] The fabricated ultrathin sheets had abundant oxygen vacancies, resulting in an improved photocatalytic performance for the aerobic oxidation of secondary amines to the corresponding imines under sunlight at room temperature. Compared to the BiOCl ultrathin nanosheets prepared through the hydrothermal process, the colloidal ultrathin sheets showed higher selectivity, conversion, and cycling stability. This improved photocatalytic performance was based on the strong absorption in the visible range and strong hydrophobic surface of the BiOCl colloidal sheets.

Recently, Xie et al.[115] revealed that significant electron–hole interactions can be produced in BiOBr owing to its restrained layered structure, which result in robust excitonic properties (Fig. 10). Their investigation showed that singlet oxygen can be easily generated for (001) plane-exposed BiOBr owing to the robust excitonic effects in BiBr (001), whereas H$_2$O$_2$ is the main product for BiOBr (010). The singlet oxygen produced by BiOBr (001) could assist the mild oxidation of the sulfides to the corresponding sulfoxides with an improved photocatalytic performance and high selectivity for five consecutive cycles.

4. Techniques for enhancing the photocatalytic activity of bismuth halides

4.1 Elemental doping

4.1.1 Transition metal doping. As dopants, transition metal ions may produce lattice defects in semiconductors or alter their crystal structure to avoid electron–hole pair
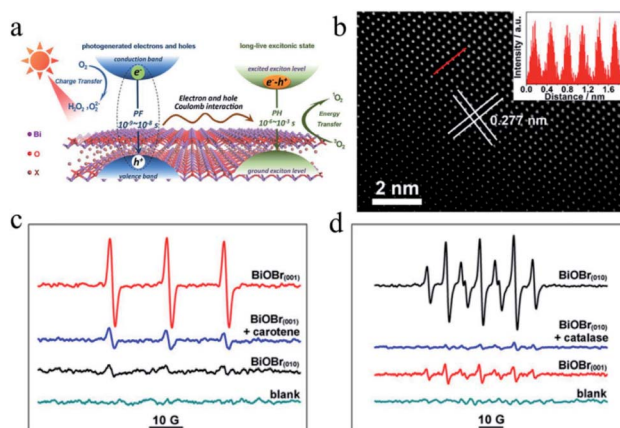

Fig. 10 (a) Schematic illustration of optical relaxation excitation processes presented in confined layered structure systems, where PH and PF are phosphorescence and prompt fluorescence, respectively. (b) Atomic-resolution scanning transmission electron microscopy (STEM) image of BiOBr(001). (c and d) Electron spin resonance (ESR) spectra. Reproduced with permission from ref. 115 Copyright 2017, the American Chemical Society.

combination, and thereby create long-lasting carriers. Doping with unique metal ions will increase the region of light absorption, and the 3D subshells and variable valence configuration have a significant impact on the photoelectrochemical behavior of semiconductors. After doping with certain transition metal ions such as Fe^{3+} and Mn^{3+}, a redshift in the energy band may be observed. The incorporation of these metal ions in the crystal lattice acts as an impurity in the forbidden band of semiconductors and the observed redshift is ascribed to the transition of an electron from these impurity bands to the CB or VB. Generally, very effective doped photocatalysts are found to be transition metal ion-based semiconductors, which should meet the following criteria: (a) the dopant can trap the electron–hole pairs, besides permitting powerful local separation and (b) the captured electrons and holes can be released and migrate to the interface.[7,15,116,117]

Numerous transition metal ions such as Fe,[116,119–122] Cu,[123] Zn,[124,125] Ti,[118] Al,[126] Sn,[127] and Mn[128] have been used as dopants in BiOX materials. For instance, Mn doping in BiOCl with oxygen vacancies could reduce its bandgap and expand its optical absorption to the visible and IR regions.[129] Both theoretical first-principle calculations and experimental observations proved the reduction in bandgap and the formation of an impurity band in the forbidden region in BiOCl after doping with tungsten.[130] For example, Fe and Cu could be incorporated into the BiOCl system through the reaction between the self-doped reactive ionic liquids 1-octyl-3-methylimidazolium tetrachloroferrate ([Omim]$FeCl_4$) and [Omim]$CuCl_3$.[119] The latter reactant, *i.e.* [Omim] $CuCl_3$, in this process not only served as a source of Cl and Cu, but also behaved as a model for Cu/BiOCl microspheres. Most importantly, Jiang *et al.* prepared a BiOBr photocatalyst doped with Ti and Ag, resulting in the successful enhancement of dye degradation, as illustrated in Fig. 11.[118]

4.1.2 Rare earth ion doping. The special electronic configurations of the inner transition metals impart spectral

properties to these elements, which are not characteristic in other elements in the periodic table. This is due to the presence of 4f orbitals with a multi-electron system. Oxides of the rare earth metals possess various crystal structures, which result in highly selective adsorption, good conductivity, and thermal stability. Various energy levels are present in these rare earth metals, where photogenerated electrons and holes can be captured easily.[131] Thus, doping of these elements enhances the electron–hole pair separation, which in turn boosts the photocatalytic ability. Y-doped microspheres of BiOBr were synthesized *via* an IL-assisted solvothermal scheme, and a shift in the X-ray diffraction (XRD) peaks was observed, demonstrating the substitution of Bi by Y in the BiOBr lattice.[132] The photocatalytic activity for the degradation of RhB and ciprofloxacin under visible-light irradiation was improved in the presence of the Y-doped sample. The enhancement in the photocatalytic properties is due to the formation of a sub-band under the conduction band, where electrons are trapped, thus reducing the recombination rate of electron–hole pairs. Other rare-earth elements such as europium and erbium were also used as dopants for the BiOX system recently.[131] Dash *et al.* synthesized a photocatalyst composed of poly(vinyl alcohol)-functionalized Eu-doped BiOX nanoflakes, which demonstrates significantly enhanced RhB degradation activity.[133]

4.1.3 Non-metal doping. The optical properties of any substance are attributed to its basic electronic configuration, *i.e.*, due to the transition of an electron from a filled orbital to an empty energy level. There is also a transition of electrons from the valence to conduction bands in the case of conductors and semiconductors.[134,135] Additional extrinsic energy levels are created between the energy bandgap upon the addition of non-metal dopants. This is supported by two hypotheses: the valence band is shifted upwards to its maximum level as a result of (i) the hybridization of the valence orbitals of the non-metal elements and (ii) the localized states from the valence orbits of the non-metal elements.

Basically, in the former case, the band to band absorption occurs as a result of the transition of electrons from the recently created valence band (VB) to the conduction band (CB), whereas according to the latter hypotheses, a pristine absorption edge remains, and small absorption peaks appear in the form of a shoulder or tail.[71,80,136] Considering the case of C-doped BiOCl materials that are formed by adsorbing dopants *via* heat treatment (Fig. 12), the mechanism for the homogeneous adsorption of carbon in the crystal surface was interpreted by utilizing nanosheets of BiOCl with high {001} or {010} facet exposure.[137] Efficient homogeneous doping of hydrothermally grafted carbonaceous nanoclusters into the crystal lattice essentially depended on the facet-related surface atomic structure.[138,139]
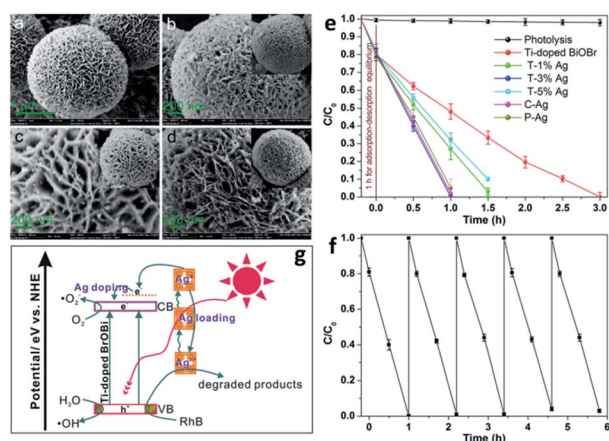
4.2 Creation of oxygen vacancies

Surface modification *via* the creation of O_2 vacancies is a fruitful method to improve the photocatalytic potential of BiOCl.[46,140,141] The electronic properties can be tuned *via* the incorporation of O_2 vacancies, which consequently improve the electron transfer and light absorption in BiOCl. For example, Guan *et al.*

Fig. 11 FESEM images of (a) as-prepared Ti-doped BiOBr microspheres, (b) C–Ag, (c) P–Ag, and (d) T–3% Ag. (e) Photocatalytic degradation of RhB over Ti-doped BiOBr. (f) Cycling runs for the photodegradation of RhB over the as-prepared T–3% Ag composites. (g) Schematic illustration of the photocatalytic mechanism of RhB degradation over T–Ag photocatalyst. Reproduced with permission from ref. 118 Copyright 2012, the American Chemical Society.
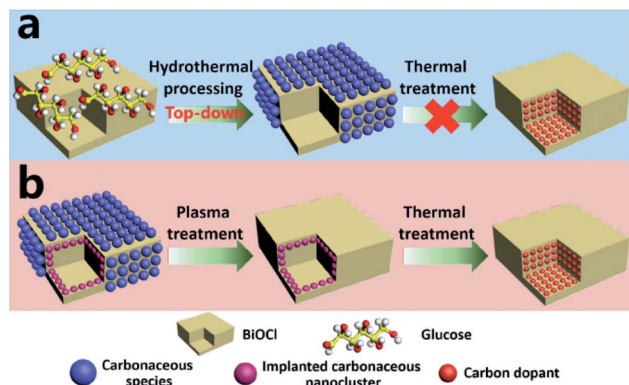
Fig. 12 (a) Exploration of the contribution of surface-modified carbonaceous species to carbon doping. (b) Elucidation of the role of implanted carbonaceous nanoclusters during carbon doping. Reproduced with permission from ref. 137 Copyright 2015, Wiley-VCH.

employed the solvothermal route to fabricate a highly thin (thickness ~2.7 nm) sheet of BiOCl and reported the associated triple vacancy as the major defect in the prepared nanosheet (Fig. 13a). Besides an enhancement in the absorption range, a reduction in the bandgap energy and exciton recombination rate was observed owing to the triple vacancy defect in BiOCl. These alterations in the electronic properties of the BiOCl nanosheet resulted in enhanced activity for the degradation of Rhodamine B dye (Fig. 13b).[142]

Another similar study was reported by Cui et al., where they prepared nanosheets of BiOCl enriched with abundant O_2 vacancies via solvothermal synthesis.[143] The generation of a new energy level (defective) upon the incorporation of O_2 vacancies was confirmed both theoretically and experimentally. This enabled photocatalytic oxygen evolution under visible light

Fig. 13 Schematic representation of the trapped positrons of (a) $V_{Bi}^{''}$ defect and $V_{Bi}^{''}V_O^{\bullet\bullet}V_{Bi}^{''}$ vacancy associates, respectively. (b) Comparison of the photodecomposition of Rhodamine B with ultrathin BiOCl nanosheets and BiOCl nanoplates under simulated solar irradiation. (c) Schematic illustration of the band structure of O_V-rich/poor BOC and pure BOC. (d) Surface photovoltage spectrum of O_V-rich/poor BOC and pure BOC. Current density transients of O_V-rich/poor BOC and pure BOC under visible-light irradiation are shown in the inset. (e) Nyquist impedance plots of O_V-rich/poor BOC and pure BOC. Reproduced with permission from ref. 142 Copyright 2013, the American Chemical Society, and ref. 143 Copyright 2018, The Royal Society of Chemistry.

irradiation by enhancing the absorption range of BiOCl films from the UV to visible region. Moreover, the increased number of O_2 vacancies offered a large photocurrent and superior charge transfer compared to BiOCl with fewer O_2 vacancies (Fig. 13d and e), respectively.

4.3 Heterojunction construction

The construction of a heterojunction is considered to be an effective way to enhance the photocatalytic activity of bismuth oxyhalides. Constructing a heterojunction at the interface of different semiconductor materials can promote the separation of photogenerated charges in the photocatalytic system.[144–147] There are various types of heterojunctions such as the conventional, direct Z-scheme, 2D/3D, and P–N heterojunctions.[97] The conventional semiconductor heterojunction (type II) is the most studied type due to its appropriate band edge location, which generates effective charge separation.[148–153] Peng et al.[154] prepared $Bi_{12}O_{17}Br_2/Bi_{24}O_{31}Br_{10}$ type-II heterojunctions via the calcination of $BiOBr/Bi(OHC_2O_4)\cdot 2H_2O$. Due to the rapid electron–hole separation in the type-II heterojunction, $Bi_{12}O_{17}Br_2/Bi_{24}O_{31}Br_{10}$ exhibited excellent photocatalytic activity for the degradation of RhB and phenol. Generally, bismuth oxyhalide nanomaterials may play three important roles in semiconductor heterojunction systems. Initially, bismuth oxyhalides have a wide range of band redox potentials, and thus they can easily match various semiconductors in energy level, which provides a driving force for the directional separation of photogenerated charges.

Next, narrow band gap bismuth oxyhalide semiconductors (BiOI and BiOBr) can be used to photosensitize other semiconductors to effectively utilize solar energy. For example, BiOI with TiO_2 and ZnO was coupled to construct p–n heterostructures via a simple chemical bath method at low temperature.[155,156] By adjusting the molar ratio of Bi to Ti/Zn, the morphology, chemical composition, and photoresponse range of the TiO_2/BiOI and ZnO/BiOI heterostructures can be carefully controlled. Compared with TiO_2 and ZnO, the more negative conduction band level of BiOI will result in the effective transfer of photogenerated electrons between the catalysts, which may prolong the lifetime of photogenerated charges and reduce the probability of photogenerated charge recombination (Fig. 14). Finally, due to the structural diversity of bismuth oxyhalides, carbon-based nanomaterials can be easily coupled with bismuth oxyhalides, which can partly increase the charge separation and transfer.[157,158] For instance, BiOCl/graphene, BiOBr/graphene, and BiOI/graphene have been utilized due to the enhanced bond between bismuth oxyhalide and graphene.[159,160] Besides, graphene can be used as a co-catalyst to extract photogenerated electrons. Therefore, the electron transfer from bismuth oxyhalides to graphene can effectively inhibit the electron–hole recombination, prolong the carrier lifetime and improve the photocatalytic efficiency. Above all, the heterojunction strategy is often used to construct binary or multicomponent composite photocatalyst systems, which is one of the universal strategies in solar photocatalysis and photoelectrocatalysis.[117]
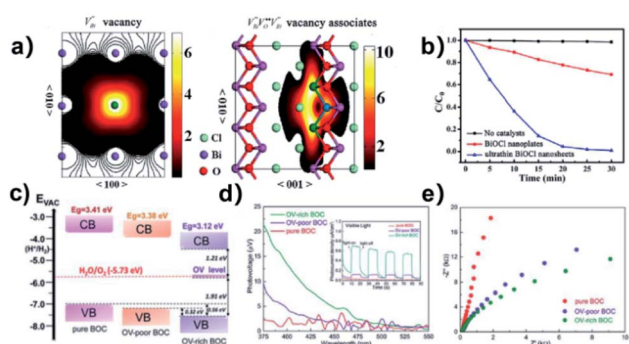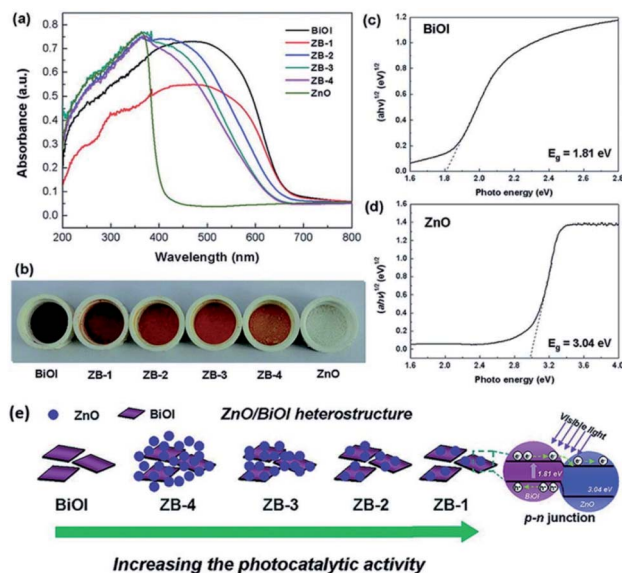
Fig. 14 (a) UV-vis diffuse reflectance spectra and (b) corresponding colors of pure BiOI, pure ZnO, and ZnO/BiOI heterostructures. Plots of $(\alpha h\nu)^{1/2}$ *versus* energy (*hν*) for the band-gap energies of (c) BiOI and (d) ZnO. (e) Schematic illustration of ZnO/BiOI heterostructures with different Bi/Zn molar ratios. Reproduced with permission from ref. 155 Copyright 2011, the American Chemical Society.

4.4 Strain modulation

The synthesis of bismuth oxyhalides is very sensitive to strain perturbation due to their specific 2D layered structure.[162] Also, the electronic structure of bismuth oxyhalides may change greatly even with the existence of subtle inner strain variation. This was investigated by Du and co-workers, who found how strain affects the photocatalytic performance over a BiOBr-square and BiOBr-circle.[161] Based on HRTEM images, they initially observed some in-plane wrinkles in the BiOBr-square, and then obtained an inhomogeneous strain distribution from GPA simulation (Fig. 15a).[161,163] This type of local lattice distortion was proven to be certainly located on the BiOBr-
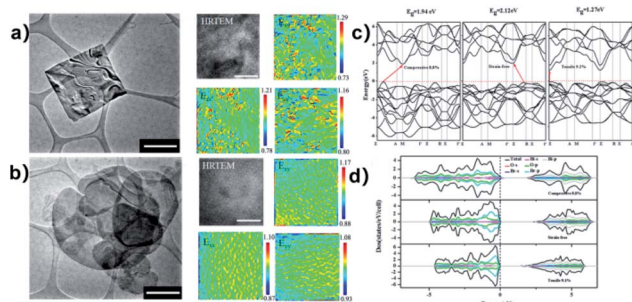

Fig. 15 (a) TEM image and simulated strain distribution based on HRTEM over a BiOBr square. The scale bar is 10 nm. (b) TEM image and simulated strain distribution based on HRTEM over a BiOBr square. The scale bar is 10 nm. (c) Band structure of BiOBr with biaxial strain calculated by DFT. (d) Calculated DOS of BiOBr with different types of strain. Reproduced with permission from ref. 161 Copyright 2015, the American Chemical Society.

square. On the contrary, the strain distribution was found to be homogeneous on the surface of the BiOBr-circle (Fig. 15b), suggesting much less lattice distortion than that in the BiOBr-square. Overall, it was clear that the strain in the BiOBr-square was much stronger than that in the BiOBr-circle. Meanwhile, the strain effect on the electronic structures was carefully studied through DFT calculations.[164] As shown in Fig. 15c and d, two types of stains (tensile strain and compressive strain) could promote the solar-light harvesting abilities in a wide range by narrowing the band gap of the photocatalysts.

4.5 Co-catalyst

In semiconductor photocatalysts, loading of co-catalysts plays a crucial role, which behave as reaction active sites and also facilitate the trapping of photogenerated charges, and hence the photocatalytic response can be significantly enhanced.[165,166] Co-catalysts formally include the deriving-electron-type (Ag, Pt, Au, MoS$_2$, and Ni) and deriving-hole-type (PbO$_2$, MnO$_x$, and NiO). It was reported that Bi$_{24}$O$_{31}$Br$_{10}$ loaded with silver nanoparticles exhibited increased photocatalytic activity in contrast with bare Bi$_{24}$O$_{31}$Br$_{10}$ and P25.[167] More recently, Zhang and co-workers demonstrated Bi$_{12}$O$_{17}$Cl$_2$ monolayers with MoS$_2$ nanosheets with the aid of noble metal co-catalysts (Fig. 16).[167] Notably, monolayers (MoS$_2$/Bi$_{12}$O$_{17}$Cl$_2$) result in a higher rate of H$_2$ production. These outcomes suggest that the use of co-catalysts serves as a suitable technique for the development of highly proficient Bi$_x$O$_y$X$_z$ photocatalysts. However, the relevant literature regarding this strategy is scarce.

4.6 Solid solution

Constructing solid solutions is an effective way to tune the band gap structure, crystal structure, and local electronic structure of materials. Due to the varying proportional range of the components, it is promising to synthesize solid-solution photocatalysts with enhanced photocatalytic activity.[168] For example, it has been widely reported that BiOCl$_{1-x}$Br$_x$, BiOBr$_{1-x}$I$_x$, and BiOCl$_{1-x}$I$_x$ solid solutions have much higher photocatalytic activity than their individual compounds.[169,170] However, due to the non-uniform synthesis conditions, little work has been performed on bismuth-rich Bi$_x$O$_y$X$_z$ solid
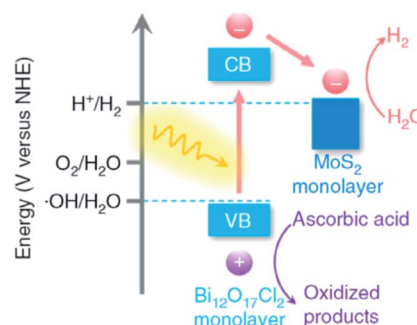

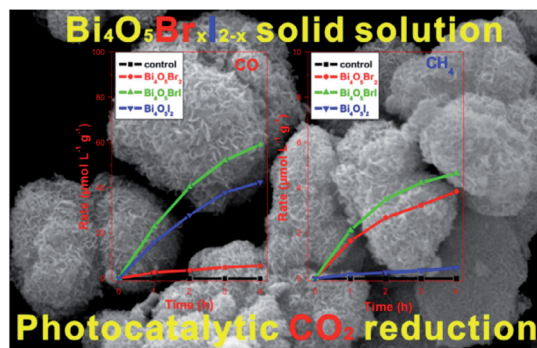**Fig. 16** Band alignments in 1L-BOC and 1L-MS. Reproduced with permission from ref. 167 Copyright 2016, Springer Nature.

Fig. 17 Photocatalytic activity for the reduction of CO_2 over hierarchical bismuth-rich $Bi_4O_5Br_xI_{2-x}$ solid solutions. Reproduced with permission from ref. 66 Copyright 2017, Elsevier B.V.

solutions. In 2015, Liu *et al.* reported the synthesis of $Bi_{24}O_{31}$-Cl_xBr_{10-x} solid solutions using a solvothermal method for the first time,[171] where the Bi_4O_5BrI solid solution with the optimal ratio ($x = 1$) displayed the highest photocatalytic activity for the photocatalytic reduction of CO_2 and Cr(VI) under visible light irradiation (Fig. 17).[66] This may be attributed to its higher CB edges than that of the other $Bi_4O_5Br_xI_{2-x}$ photocatalysts. These results clearly demonstrate that the formation of solid solutions is an effective method to modify the energy structure and enhance the photocatalytic performance of $Bi_xO_yX_z$.

4.7 Composite framework

4.7.1 Bismuth oxyhalide-based binary composites. Recently, the impressive photocatalytic activity and remarkable structures of BiOX-based photocatalysts have gained increasing attention.[20,146,172–175] BiOX possess a $[Bi_2O_2]^{2+}$ coating assembly of crystals surrounded by halogen atom slabs. Additionally, the internal electric field (static) present between two layers filled with separated photo-induced electrons and holes improves its photocatalytic performance.[176,177] ZnO is considered an effective photocatalyst for the purification of water.[178–186] However, its wide bandgap energy (3.2 eV) restricts its photocatalytic performance to the UV region.[187–191] Thus, to enhance its photocatalytic performance and ability to absorb sunlight, different photocatalyst composites (ZnO/BiOX) have been synthesized.[155,192–194] Geng *et al.* prepared various BiOBr/ZnO materials through the hydrothermal method for the removal of methylene blue (MB) in the aqueous phase.[177] Suspended $Zn(OH)_2$ was prepared by adding $Zn(NO_3)_2 \cdot 6H_2O$ to a KOH solution, and in a separate beaker, a specific concentration of KBr with $Bi(NO_3)_3 \cdot 5H_2O$ was dripped in water (deionized), and the resulting mixture was added dropwise to the above solution at pH 7 with continuous stirring. Then, the obtained solution was autoclaved for 12 h at 120 °C. The EDS spectrum of BiOBr/ZnO confirmed that the sample contained Br, O, Bi, and Zn and the construction of a heterojunction (Fig. 18a). Due to the interaction among BiOBr and ZnO, the symmetry of heterojunction did not change during the preparation, as revealed by the TEM images (Fig. 18b). HR-TEM (Fig. 18c) indicated a lattice spacing of 0.284 nm {102} and 0.264 nm {002} for ZnO and BiOBr,
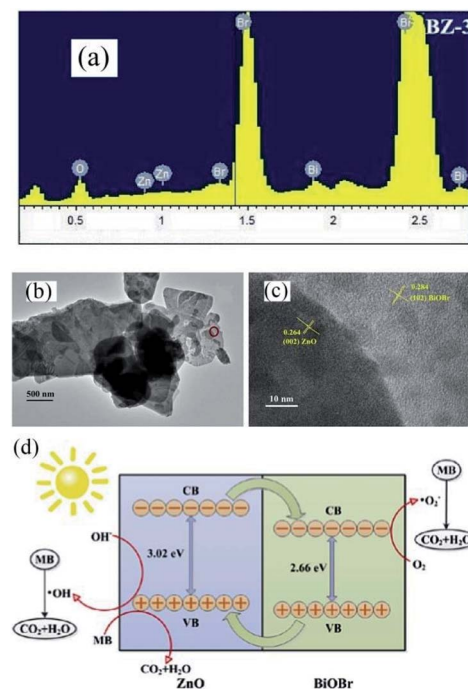

Fig. 18 (a) EDS pattern, (b) TEM image, (c) HRTEM image, and (d) photocatalytic mechanism of BiOBr/ZnO heterojunction. Reproduced with permission from ref. 177 Copyright 2017 Elsevier B.V.

respectively, and the formation of heterojunction BiOBr. The photocatalytic activity improved due to the formed heterojunction given that it reduced the recombination rate of light-generated excitons. The synthesized heterojunction of BiOBr/ZnO mirrored the Z-scheme process for dye (MB) degradation (Fig. 18d).[177] Consequently, the formed O_2^- decomposed the dye (MB) molecules into CO_2 and H_2O.

4.7.2 Bismuth oxyhalide-based ternary composites. Nowadays, metal oxides with multiple components have attracted significant attention for water purification *via* photocatalysis.[195] Recently, $CdWO_4$,[196] $BiWO_4$,[197] and $ZnWO_4$,[198] which are ternary metal oxides, have been utilized as photocatalysts under visible light. Cao *et al.* fabricated a $CdWO_4$/BiOBr photocatalyst based on visible light through a hydrothermal and chemical precipitation process for the degradation of RhB dye.[196] During the synthesis of $CdWO_4$/BiOBr, a certain amount of $Bi(NO_3)_3 \cdot 5H_2O$ and KBr amount was dissolved in solution, while $CdWO_4$ was observed as a suspended component. Further, the obtained solution was kept for 5 h at 80 °C on a water bath. $CdWO_4$/BiOBr composites were synthesized with 5%, 15%, and 25% molar ratios of $CdWO_4$ in $CdWO_4$/BiOBr. The sample that showed the maximum degradation of RhB under visible light in 8 min was the 15% molar ratio. This sample exhibited the maximum performance for degradation compared to the individual BiOBr and $CdWO_4$ photocatalysts. The p–n junction promoted electron–hole pair separation, which improved the catalytic activity of the composite. A $BiVO_4$/BiOCl composite was synthesized by Ma *et al. via* a hydrothermal process for the degradation of norfloxacin. $BiVO_4$ and PVP were stirred for homogeneous mixing together with concentrated HCl (0.7, 0.5, 0.3, and 0.1).[199]
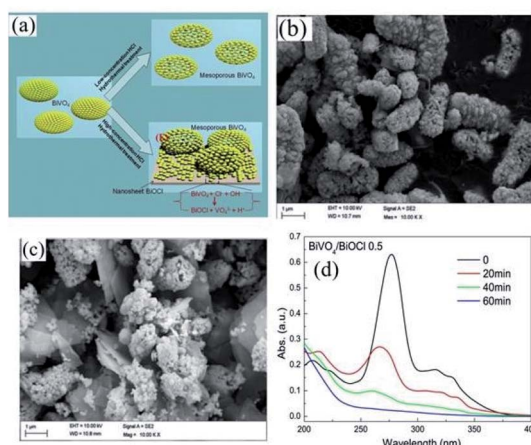
Fig. 19 (a) Formation of BiOCl nanosheets over BiVO₄/BiOCl heterojunction. TEM image of BiVO₄/BiOCl heterojunction at (b) 0.1 HCl and (c) 0.5 HCl concentration. (d) Photocatalytic activity of BiVO₄/BiOCl-0.5 heterojunction for the degradation of norfloxacin. Reproduced with permission from ref. 199 Copyright 2017, Elsevier B.V.

The mixture was further heated in an autoclave at 180 °C for 10 h (Fig. 19a). The structure obtained was mesoporous at a concentration of 0.1 M HCl. The TEM images displayed nanosheets of the BiVO₄/BiOCl composite at different concentrations of HCl. However, although nanosheets were obtained for 0.1 M HCl concentration (Fig. 19b and c), the nanosheets formed for 0.5 M HCl concentration showed the maximum photocatalytic activity under visible light for the degradation of the norfloxacin antibiotic, which was caused by the formation of a p–n junction in 1 h between the composite (Fig. 19d). As mentioned above, the formation of a p–n junction restricted the recombination of charge carriers, which resulted in an enhancement in photocatalytic activity.

4.7.3 CNT-based bismuth oxyhalide composites. Carbon nanotubes (CNTs) have been well developed due to their effective conductivity, capture capability, and high electron affinity. Many researchers reported an enhancement in photocatalytic efficiency caused by the addition of CNTs in nanocomposites. The use of carbon-based materials can also be an efficient strategy to enhance photocatalytic efficiency. For instance, Xu *et al.* reported the synthesis of hierarchical structure BiOX (X = Cl/I) NSs *via* an ionic layer adsorption and reaction method, which showed notable photocatalytic activity for the degradation of Methyl Orange (MO).[19] Improved stability and recycling ability under simulated sunlight were observed. As presented in Fig. 20a, the CNTs act as a promising material to tailor the energy gaps of semiconductors *via* covalent bonds due to their excellent mechanical properties and high pollutant absorption ability. A similar result was described by Xiong *et al.*, where BiOI–MWCNT composites synthesized *via* an EG-assisted solvothermal method exhibited higher visible-light photocatalytic activity than that of BiOI, which can be attributed to the interfacial charge-transfer, as shown in Fig. 20b.[200] Due to its extensive specific surface area and the promising charge transfer properties, the CNT–BiOI composite can be used as
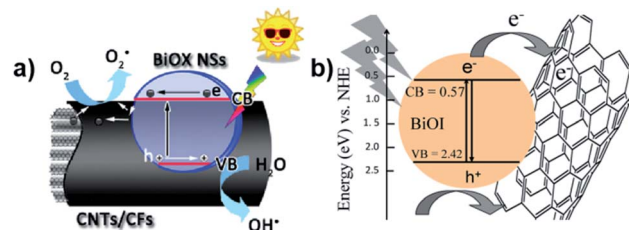

Fig. 20 (a) Photocatalytic mechanism of the hierarchical CNT/CF-BiOX NS structures. (b) Photoinduced electron transfer between an excited BiOI particle and MWCNT and charge equilibration. Reproduced with permission from ref. 19 Copyright 2014, Springer Nature and ref. 200 Copyright 2012, Elsevier B.V.

a highly efficient and delicate system for the degradation of organic pollutants.

4.7.4 Graphene-based bismuth oxyhalide composite. Graphene displayed an array of advantages in photocatalytic composite systems in recent decades as a conventional layered material. Li *et al.*, for example, reported the one-pot synthesis of a composite of BiOBr–graphene with significantly enhanced photocatalytic activity for the degradation of Rhodamine B (RhB), which simultaneously exhibited excellent dye absorption, intense charge-separation, and transport properties.[129] In this work, graphene oxide could be reduced to graphene *via* the solvothermal method, and the BiOBr particles were found to grow on the graphene surface simultaneously, as illustrated in Fig. 21a. Moreover, the functional graphene–BiOBr composites exhibited novel properties owing to the combination of the advantages of graphene nanosheets and BiOBr. Zhang *et al.* found that modified RGO/BiOCl nanocomposites showed 8.4-times and 3.8-times greater activity enhancement for the degradation of MO and oxidation of water than that of BiOCl, respectively, which was attributed to the enhanced charge separation and extended carrier lifetime of BiOCl by chemically bonding with RGO.[201] Interestingly, the results in this study indicated that chloride vacancies act as recombination centers, which may impede photogenerated charge separation, as shown in Fig. 21b. In addition, it has also been reported that Er-doped BiOBr–graphene hollow microspheres exhibited a major improvement in photocatalytic activity for the degradation of RhB under simulated sunlight irradiation, which may be due to the strong synergistic effect between charge separation and solar energy harvesting.[202] In summary, compared with other layered materials, graphene is much more appealing to exactly regulate the behaviors of photogenerated electrons and holes in bismuth oxyhalide-based composite photocatalysis systems, largely due to its flexible atom-thin 2D nature, unique electronic properties and excellent absorptivity, which are promising candidates in photocatalysis.[203]

4.8 Plasmonic material-supported photocatalysts

Surface plasmon resonance (SPR) is a phenomenon involving electromagnetic oscillation produced on the surface of a metal *via* the interaction of free electrons and photons. Surface plasmons have many distinctive properties due to the association
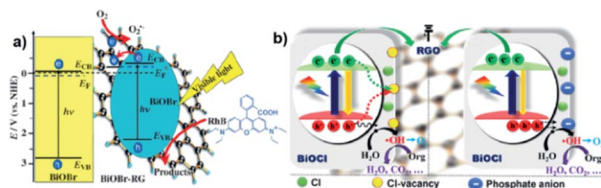
Fig. 21 (a) Schematic illustration of energy-band diagrams of BiOBr and BiOBr–RG, schematic structure of BiOBr–RG, and tentative processes of the photodegradation of RhB over BiOBr–RG. (b) Proposed mechanism for the photogenerated charge transfer and separation in RGO/BOC photoanodes before and after phosphate modification. Reproduced with permission from ref. 204 Copyright 2012 Wiley-VCH and ref. 201 Copyright 2012, Elsevier B.V.

Fig. 23 (a) H_2 evolution mechanism and (b) free energy diagram for HER occurring on the (001) basal plane of single-layer BiOX. Reproduced with permission from ref. 207 Copyright 2019, the American Chemical Society.

between surface charge oscillation and lightwave electromagnetic field. As the light pulse (electromagnetic wave) enters the metal–dielectric interface, the free electrons collectively oscillate on the metal surface. Then, the electromagnetic wave is coupled with the free electrons on the metal surface to form a type of near-field electromagnetic wave propagating along the metal surface. When the oscillation frequency of the electron is close to or consistent with the frequency of the incident light wave, resonance will occur, which makes the metal absorb and scatter the incident light strongly and causes resonance extinction. In the resonance state, the energy of the electromagnetic field is effectively transformed into the collective vibration energy of the free electrons on the metal surface. Meanwhile, a special electromagnetic mode is formed, where the electromagnetic field is confined to a small area of the metal surface and is significantly enhanced (that is, the intensity of the local electric field generated near the metal is much stronger than that of the incident light), which is defined as surface plasmon resonance (Fig. 22).[205,206]

5. Theoretical studies

5.1 H_2 production

Recently, Pan et al.[207] used DFT calculations discover the source of catalysis on single-layer BiOX (Fig. 23a). The core possible calculations proposed that the single-layer BiOX-Bi and BiO-terminations are constant in O-poor and O-rich conditions, respectively. The Bi and BiO-terminations of single-layer BiOX were observed to have distinct HER active sites, while the (001) basal planes are inert. The Gibbs free energies (GFE) are similar to the optimum values of 0 eV for the H-atoms adsorption on Bi-
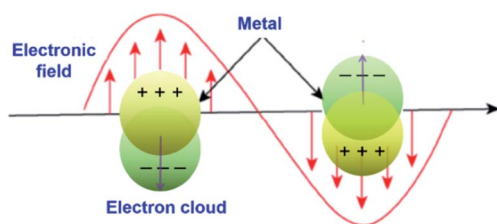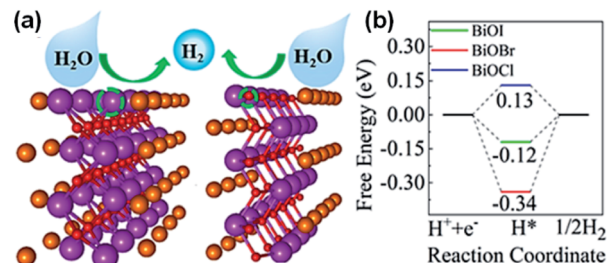
and BiO-terminations, signifying that there are favorable HER performances for single-layer BiOX (Fig. 23b). These termination-enhanced HER behaviors are attributed to the clustered edge states around the Fermi stage induced by the Bi 6p fringe bismuth atom orbital density and O 2p fringe oxygen atom orbital density, respectively.

5.2 O_2 production

Further, oxygen can be generated by doping BiOCl with elemental sulfur and the sacrificial reagent $AgNO_3$ under UV-vis irradiation.[208] Thus, by doping BiOCl with sulfur, the photogenerated charge carrier separation efficiency boosts the evolution of oxygen by five times than in BiOCl. For improving strength of IEF, allowing 80% charge splitting efficiency by directing it, BiOCl and homogeneous carbon-doped Bi_3O_4Cl nanosheets were fabricated.[209] Femtosecond-resolved transient absorption spectroscopy showed that the strong IEF separated the electron–hole pairs restricted within the $[Bi_3O_4]$ and [Cl] slices when they drifted from the bulk to surface. Finally, water could be split to give out oxygen with an efficiency of about 90 $\mu mol\ h^{-1}$ when 0.1 g of Bi_3O_4Cl nanosheets doped with carbon was dispersed in 200 mL water in the absence of a co-catalyst and electron-scavenger under visible light (150 W Xe arc lamp equipped with a 420 nm cutoff filter). However, the Bi_3O_4Cl nanosheets doped with carbon were not able to generate hydrogen given that their conduction band is more positive than the activation potential of H_2. O_2 was generated by heterostructure photocatalysts (mechanism shown in Fig. 24a with DFT calculations) of Bi_3O_4Cl/BiOCl with a Z-scheme by Lin et al.[210] (synthesis procedure shown in Fig. 24b). They suggested an operative method to promote the photocatalytic O_2 progress through the dual-induced {0 0 1} plane of BiOCl nanosheet heterostructures. Using an electron scavenger ($AgNO_3$ and $FeCl_3$), O_2 was produced at a rate of 58.6 $\mu mol\ g^{-1}\ h^{-1}$ by Bi_3O_4Cl/BiOCl (Fig. 24c and d).

5.3 CO_2 production

DFT calculations verified that for the band structure, oxygen vacancies introduce impurity levels among the valence and conduction band of BiOCl. The introduction of impurity levels is the intention for the absorption of visible and infrared light for
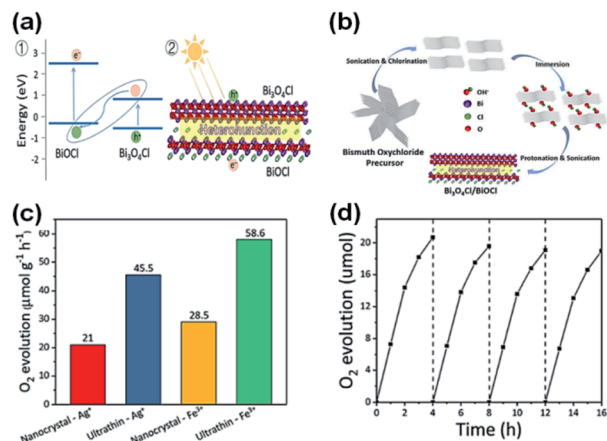

Fig. 22 Schematic illustration of surface plasmon resonance (SPR) on the metal surface.

Fig. 24 (a) Band alignment for ultrathin $Bi_3O_4Cl/BiOCl$ heterostructures (a type-II heterojunction) by theoretical calculation. (b) Synthetic route for the fabrication of the $Bi_3O_4Cl/BiOCl$ heterostructures. (c) Demonstration of an ultrathin $Bi_3O_4Cl/BiOCl$ with a Bi_3O_4Cl monolayer lying on top of a BiOCl monolayer. Photogenerated charge carriers separated into different layers. (c) O_2 evolution rates of pure BiOCl, nanocrystal $Bi_3O_4Cl/BiOCl$, and ultrathin $Bi_3O_4Cl/BiOCl$. (d) O_2 rate with respect to time. Reproduced with permission from ref. 210 Copyright 2019, Wiley-VCH.

BiOC with oxygen vacancies (BOC-OV).[211] Moreover, DFT calculations evidenced that for the case of $BiOV_4$, the vanadium vacancies introduce impurity levels similar to that of BOC-OV.[5] Additionally, density of states (DOS) studies showed that the CO_2 conversion performance of photocatalysts based upon Bi is merely based on the thickness of the catalyst. Similar to its bulk counterpart, the few-layered Bi_2WO_6 structure possess an amplified DOS at the CBM, as presented in Fig. 25a and b.[212] The thickness of the catalyst also causes the DOS of BiOI to fluctuate, given that the CBM and VBM of bulk BiOI are lower than that of few-layered BiOI, which is quite higher in previous reports. Bismuth-rich Bi–O–X revealed a similar relation, given that the CBM of compounds based on Bi generally contains 6p orbitals for Bi. According to the DOS calculations, the order of the CBM is $Bi_xO_yBr \gg BiOBr$, which reveals the greater capacity of Bi_xO_yBr for the photoreduction (using visible light) of CO_2 to hydrocarbon fuel.[104,212,213]

Additionally, the change in the performances for the photocatalytic reduction of CO_2 with different planes was shown by DOS calculation. It exhibited that the (001) plane for BiOI has a more positive CBM capacity compared to the (100) plane of BiOI for the reduction of CO_2.[214] Further, the (100) plane of $BiOIO_3$ exhibits a more negative VB compared to the (010) plane of $BiOIO_3$, which displays a more positive CB. Hence, excitons are transferred to the (010) and (100) planes, respectively.[215] The transfer of electrons among dissimilar planes of BiOCl can boost the charge migration, resulting in higher activity, as displayed in Fig. 25c and d.[87] For a better understanding of the possible reaction paths of CO_2 conversion, an investigation on the transient state of CO_2 using a photocatalyst based on Bi was performed. As an example, the photocatalytic dissociation path of CO_2 between various crystalline planes of Bi_2WO_6 was reported. Thermodynamically greater stability was achieved for CO_2 adsorbed on the Bi_2WO_6 planes compared to that of non-
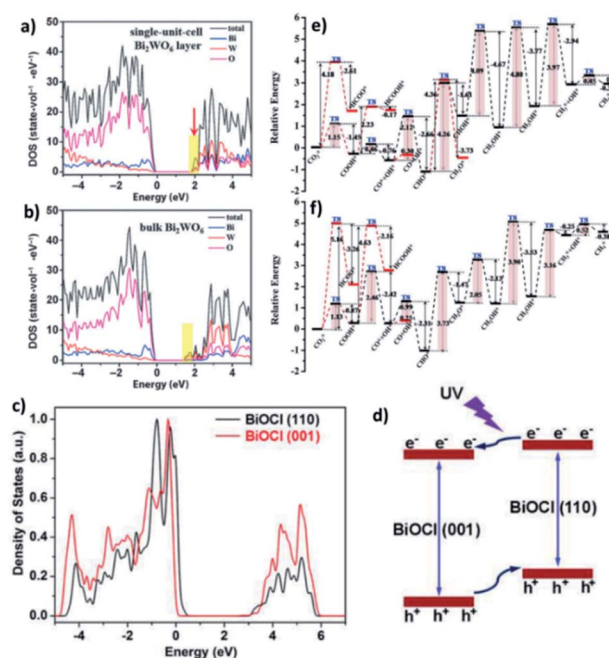

Fig. 25 (a) DFT calculations of Bi_2WO_6 single-unit-cell layer slab and (b) bulk Bi_2WO_6 slab. Reproduced with permission from ref. 213 Copyright 2015, Wiley-VCH. (c) PDOS diagrams from first-principles simulations for BiOCl (001) and (110) facets and (d) schematic showing the facet-dependent charge migration propensities in BiOCl. Reproduced with permission from ref. 87 Copyright 2015, Wiley-VCH. (e and f) Reaction pathways for CO_2 reduction to CH_4 on BOC-OV and BOC, respectively, where "*" represents adsorption on the substrate. The red route is the alternative pathway. Reproduced with permission from ref. 211 Copyright 2017, The Royal Society of Chemistry.

adsorbed CO_2. However, thermodynamic instability was observed for CO–O adsorption on the (001) plane. Meanwhile, the energy barrier of the Bi_2WO_6 (101) facets is higher compared to that of the Bi_2WO_6 (001) planes and spontaneous CO_2 dissociation without photocatalysis. Therefore, the most thermodynamically favoured planes for photocatalytic CO_2 reduction are the Bi_2WO_6 (001) planes.[216] A higher energy barrier was observed for the direct dissociation of CO_2 compared to CO_2 hydrogenation dissociation. Additionally, the energy barrier of COOH is lower compared to HCOO with respect to the (001) planes on both BOC and BOC-OV. Hence, CO_2 hydrogenation to COOH offers the best thermodynamically favored mechanism of CO_2 reduction. Besides, the low energy barrier clarifies that CO is the main product of CO_2 reduction on BOC and BOC-OV, as shown in Fig. 25e and f, respectively. Likewise, the hydrogenation of CH_2OH* is the rate-determining step in the CH_4*-generation path. Therefore, the formation of CH_4 is not energetically favored. Furthermore, the rate-determining step of CO formation is the hydrogenation of CO_2.[211]

5.4 N₂ fixation

Ye et al.[217] developed 5 nm-diameter nanotubes of Bi_5O_7Br via a self-assembly approach. In the Bi_5O_7Br nanotubes, oxygen vacancies could be generated to give plenty of localized electrons to activate N_2 under the light irradiation. These nanotubes
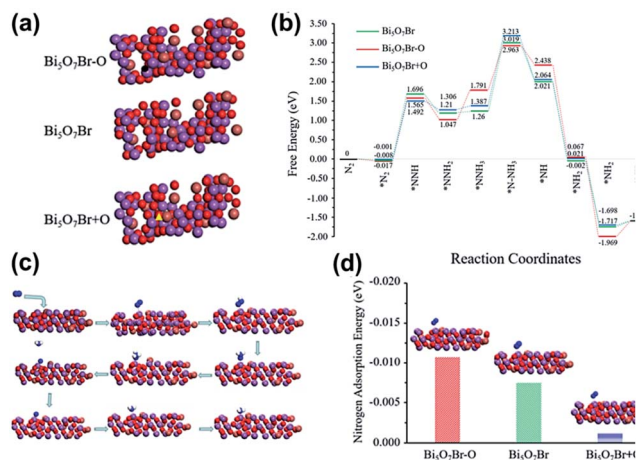
Fig. 26 (a) Structures of anoxic Bi$_5$O$_7$Br−O, pristine Bi$_5$O$_7$Br, and oxygen-enriched Bi$_5$O$_7$Br + O. Black circle and yellow triangle represent oxygen vacancy sites and additional oxygen sites, respectively. (b) Reaction energy diagram of N$_2$ fixation catalyzed by Bi$_5$O$_7$Br−O, Bi$_5$O$_7$Br and Bi$_5$O$_7$Br + O. (c) N$_2$ fixation process. (d) N$_2$ adsorption energy on the surfaces of Bi$_5$O$_7$Br−O, Bi$_5$O$_7$Br and Bi$_5$O$_7$Br + O. Reprinted with permission from ref. 218 Copyright 2020, the American Chemical Society.

effectively reduced N$_2$ to NH$_3$ in water at a of rate up to ~1.38 mmol g^{-1} h^{-1} under visible light. The apparent quantum efficiency at 420 nm exceeded 2.3%. Also, no obvious loss in activity was observed during four-fold cycle tests. Recently, Xiong et al.[218] showed that the NH$_3$ generation rates could be extended to 12.72 mmol g^{-1} h^{-1} under visible light (xenon bulb, 300 W) through Bi$_5$O$_7$Br nanostructures. This is highest ammonia generation rate recorded to date over a Bi$_a$O$_b$X$_c$ material (Fig. 26).

Recently, in 2021 Xue et al.[100] used a solvothermal template-free approach to synthesize Bi$_2$WO$_6$ hollow microspheres with oxygen vacancies (OVs-BWO). Ethylene glycol has the ability to scavenge terminal oxygen atoms, resulting in the formation of oxygen vacancies in the form of W^{5+} and Bi$^{(3-x)+}$ species with low oxidation states. The experimental results combined with DFT calculations showed that the optimal N$_2$ fixation with an output of 80.5 m^2 g^{-1} exhibited the ammonia yield of 106.4 μmol g$_{cat}^{-1}$ under simulated sunlight for 2 h, which was 18 times higher than equal-area nest-like Bi$_2$WO$_6$ without OVs. The enhanced activity is mainly attributed to the transfer of meta-stable electrons within the sub-band (i.e., defect energy level) induced by oxygen vacancies to the π-anti-bonding orbitals of N$_2$ via non-radiative transfer, leading to the activation of the nitrogen molecules. The activation and hydrogenation of nitrogen at the active sites of OVs-BWO surface were investigated by DFT calculation (Fig. 27). Subsequently, three possible nitrogen reduction reaction (NNR) processes on the active sites together with their corresponding rate-determining steps were proposed. The material is durable and stable, and there is almost no loss in activity after continuous repeated experiments in the nitrogen reduction process. Therefore, the OVs-BWO material provides an alternative for efficient N$_2$ fixation under ambient conditions using atmosphere and water as the feed-stock and sunlight as the driving force.
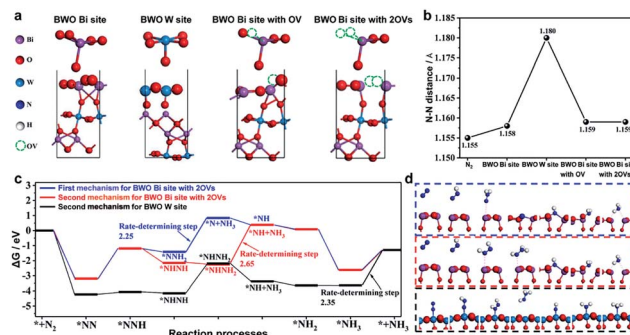

Fig. 27 (a) Models of the four possible active sites for Bi$_2$WO$_6$ (010) surface, W site, Bi site, Bi site with OV, and Bi site with 2OVs. (b) N−N distance of free N$_2$ and N$_2$ on the four possible active sites. (c) Gibbs free energy during the reaction processes via two different mechanisms (the first mechanism: * + N$_2$ → *NN → *NNH → *NNH$_2$ → *N + NH$_3$ → *NH → *NH$_2$ → *NH$_3$ → * + NH$_3$ and the second mechanism: * + N$_2$ → *NN → *NNH → *NHNH → *NHNH$_2$ → *NH + NH$_3$ → *NH$_2$ → *NH$_3$ → * + NH$_3$, where * represents the active site) and (d) the free-energy profile of three possible processes for BWO W site and BWO Bi site with 2OVs. Reprinted with permission from ref. 100 Copyright 2021, the American Chemical Society.

6. Conclusion, challenges, and future prospects

Encouraging photocatalysts for environmental and especially energy-associated applications correspond to a special class of materials that includes BiOX. The advantage of this class is its innovative structure comprised of a layered arrangement, tremendous physicochemical properties, and tunable electronic features. However, bare BiOX demonstrates some inherent drawbacks, including low light-harvesting efficiency, huge probability for the recombination of photogenerated excitons, lack of active sites for catalytic features, and lastly low specific surface area. Thus, great efforts have been dedicated to minimizing or eliminating these drawbacks, resulting in the optimization of BiOX materials for an enhancement in photocatalytic activity. The present review presented the recent developments in the design of new approaches for the preparation of BiOX materials. Additionally, we also discussed numerous schemes for the enhancement in photocatalytic activity, and finally the introduction of several BiOX-based nanocomposite frameworks with a minor focus on plasmonic-based photocatalysts. The tailoring of porous crystal structures and fabrication of ultrathin assemblies can enhance the photocatalytic activity of BiOX materials. Numerous routes have been utilized for the additional enhancement of photocatalytic activity, including elemental doping with rare earth metals, metals, and non-metals, and the generation of oxygen vacancies. BiOX-based materials are exceptional candidates for a wide range of applications involving photocatalysis. These applications include organic synthesis, oxygen and hydrogen evolution, disinfection, nitrogen fixation, pollutant removal, and reduction of CO$_2$. Therefore, significant efforts have been devoted to developing BiOX-based materials and enhancing their

photocatalytic activity; however, their, potential has not been completely exploited.

This review on 2D materials disclosed that the reduction of the thickness of these materials to the atomic level can result in intrinsic properties related to the bulk material and unique properties not visualized in the bulk material. The layered assembly of BiOX allows its facile transformation into a mono/few-layer assembly. However, additional consideration is necessary for the controlled fabrication of atomically thick BiOX. To optimize the photocatalysis process, the incorporation of defects in BiOX nanostructures has been studied. Generally, the type of defects observed in BiOX-based materials is oxygen vacancies. Various supplementary defects are not formed in nanostructures of BiOX such as dislocations, halogen vacancies, and dual vacancies. However, they may promote the transfer rate of electron and induce extra electronic states in BiOX. An enhancement in the density of states is typically aimed to enhance the photocatalytic activity of these materials. However, more effective approaches must be developed to construct different defects in BiOX and gain an in depth understanding of the relation between the type of defect and enhancement in photocatalytic activity.

Additionally, varying the content of Bi content in BiOX-based materials can be employed for the reduction of CO_2 using a photocatalytic scheme. Presently, the main products from the photoreduction CO_2 by BiOX are CH_4 and CO. A manageable Bi-rich approach can practically tune the band edge positions and bandgap energy of BiOX-based materials. Thus, it is extremely necessary to achieve extraordinary selectivity for the photoreduction products of CO_2 via the additional engineering of BiOX nanosheet materials. Despite the significant development in photocatalysts based on BiOX materials, the nature of the active catalytic sites present in these materials is still uncertain. Thus, studies on the mechanism of BiOX-based photocatalysts in numerous applications at the atomic level are desirable. Extra consideration should be dedicated to defining and calculating the active catalytic sites through the help of direct experimental measurements and calculation.

Supported co-catalysts can promote the redox reaction, especially the synergistic effect of two catalysts (deriving-electron-type (Ag, Pt, Au, MoS_2, and Ni) and derived hole-type (PbO_2, MnO_x, IrO_x, CoO_x, and NiO)). It has been reported that $Bi_xO_yX_z$ photocatalysts have high space charge separation efficiency, which can accelerate the oxidation reaction and reduction reaction rate, and subsequently result in a higher total reaction rate. However, the synthesis and application of $Bi_xO_yX_z$ photocatalysts are still challenging. Also, it is very difficult to synthesize pure bismuth-rich bismuth oxyhalides. Currently, two synthetic methods, i.e., hydrothermal alkalization and calcination, are usually applied for the preparation of bismuth-rich oxyhalide. However, a slight change in pH or temperature can lead to differences in the physicochemical properties of the $Bi_xO_yX_z$ photocatalyst. Moreover, only $Bi_4O_5X_2$ (X = Br and I) was obtained by the molecular precursor method. Therefore, it is urgent to explore new synthetic routes for the application of $Bi_xO_yX_z$ photocatalysts. Currently, photocatalysts are mainly applied in environmental remediation and solar power generation, but $Bi_4O_5X_2$ can be used in other applications such as the photocatalytic inactivation of bacteria and photocatalytic organic synthesis, which will be of great importance in the future. Meanwhile, many advanced characteristic technologies have been developed to investigate the photocatalytic mechanism of $Bi_xO_yX_z$, such as in situ infrared spectroscopy and synchrotron radiation technology, which have greatly promoted the research on $Bi_xO_yX_z$ photocatalysts.

BiOX-based materials can be further explored as nanocomposite catalysts, such as supported IB metal particles, for photocatalytic conversions to yield high-value chemicals. Notably, IB metal particles exhibit good surface plasmon resonance properties and can emerge as excellent electron acceptors for the adsorption and activation of oxygen, thus remarkably promoting photocatalytic conversions. However, more in situ characterization routes and measurements that are close to realistic situations are desirable to improve the atomic level understanding of the relationship between active catalytic sites and photocatalysis, which will be advantageous to enhance the tailored design of BiOX materials for photocatalytic applications.

Conflicts of interest

There are no conflicts to declare.

Acknowledgements

Notes and references

1 A. A. Ismail and D. W. Bahnemann, Sol. Energy Mater. Sol. Cells, 2014, 128, 85–101.

2 M. Ni, M. K. H. Leung, D. Y. C. Leung and K. Sumathy, Renewable Sustainable Energy Rev., 2007, 11, 401–425.

3 T. Hisatomi and K. Domen, Nat. Catal., 2019, 2, 387–399.

4 P. Ganguly, M. Harb, Z. Cao, L. Cavallo, A. Breen, S. Dervin, D. D. Dionysiou and S. C. Pillai, ACS Energy Lett., 2019, 4, 1687–1709.

5 S. Gao, B. Gu, X. Jiao, Y. Sun, X. Zu, F. Yang, W. Zhu, C. Wang, Z. Feng, B. Ye and Y. Xie, J. Am. Chem. Soc., 2017, 139, 3438–3445.

6 L. Liang, F. Lei, S. Gao, Y. Sun, X. Jiao, J. Wu, S. Qamar and Y. Xie, Angew. Chem., Int. Ed., 2015, 54, 13971–13974.

7 J. Xiong, P. Song, J. Di and H. Li, J. Mater. Chem. A, 2020, 8, 21434–21454.

8 D. S. Bhachu, S. J. A. Moniz, S. Sathasivam, D. O. Scanlon, A. Walsh, S. M. Bawaked, M. Mokhtar, A. Y. Obaid, I. P. Parkin, J. Tang and C. J. Carmalt, Chem. Sci., 2016, 7, 4832–4841.

9 M. Ikram, A. Raza, M. Imran, A. Ul-Hamid, A. Shahbaz and S. Ali, Nanoscale Res. Lett., 2020, 15, 95.

10 S. Cao, L. Piao and X. Chen, Trends Chem., 2020, 2, 57–70.

11 Z. Wei, J. Liu and W. Shangguan, Chin. J. Catal., 2020, 41, 1440–1450.

12 P. Chiesa, S. Consonni, T. Kreutz and W. Robert, *Int. J. Hydrogen Energy*, 2005, **30**, 747–767.

13 N. Fajrina and M. Tahir, *Int. J. Hydrogen Energy*, 2019, **44**, 540–577.

14 U. Gupta and C. N. R. Rao, *Nano Energy*, 2017, **41**, 49–65.

15 J. Di, J. Xia, H. Li, S. Guo and S. Dai, *Nano Energy*, 2017, **41**, 172–192.

16 J. Di, J. Xia, M. Ji, L. Xu, S. Yin, Q. Zhang, Z. Chen and H. Li, *Carbon*, 2016, **98**, 613–623.

17 Y. Zhou, W. Wang, C. Zhang, D. Huang, C. Lai, M. Cheng, L. Qin, Y. Yang, C. Zhou, B. Li, H. Luo and D. He, *Adv. Colloid Interface Sci.*, 2020, **279**, 102144.

18 A. Raza, M. Ikram, M. Aqeel, M. Imran, A. Ul-Hamid, K. N. Riaz and S. Ali, *Appl. Nanosci.*, 2020, **10**, 1535–1544.

19 B. Weng, F. Xu and J. Xu, *J. Nanopart. Res.*, 2014, **16**, 2766.

20 K. Sharma, V. Dutta, S. Sharma, P. Raizada, A. Hosseini-Bandegharaei, P. Thakur and P. Singh, *J. Ind. Eng. Chem.*, 2019, **78**, 1–20.

21 X. Zhang, Z. Ai, F. Jia and L. Zhang, *J. Phys. Chem. C*, 2008, **112**, 747–753.

22 X. Jin, L. Ye, H. Xie and G. Chen, *Coord. Chem. Rev.*, 2017, **349**, 84–101.

23 G.-J. Lee, Y.-C. Zheng and J. J. Wu, *Catal. Today*, 2018, **307**, 197–204.

24 X. Wang, C. Zhou, L. Yin, R. Zhang and G. Liu, *ACS Sustainable Chem. Eng.*, 2019, **7**, 7900–7907.

25 J. Li, H. Li, G. Zhan and L. Zhang, *Acc. Chem. Res.*, 2017, **50**, 112–121.

26 Y. Wang, Y. Long and D. Zhang, *ACS Sustainable Chem. Eng.*, 2017, **5**, 2454–2462.

27 D. Kato, K. Hongo, R. Maezono, M. Higashi, H. Kunioku, M. Yabuuchi, H. Suzuki, H. Okajima, C. Zhong, K. Nakano, R. Abe and H. Kageyama, *J. Am. Chem. Soc.*, 2017, **139**, 18725–18731.

28 A. M. Ganose, M. Cuff, K. T. Butler, A. Walsh and D. O. Scanlon, *Chem. Mater.*, 2016, **28**, 1980–1984.

29 D. Kandi, S. Martha, A. Thirumurugan and K. M. Parida, *J. Phys. Chem. C*, 2017, **121**, 4834–4849.

30 R. Dong, Y. Hu, Y. Wu, W. Gao, B. Ren, Q. Wang and Y. Cai, *J. Am. Chem. Soc.*, 2017, **139**, 1722–1725.

31 C. Lai, M. Zhang, B. Li, D. Huang, G. Zeng, L. Qin, X. Liu, H. Yi, M. Cheng, L. Li, Z. Chen and L. Chen, *Chem. Eng. J.*, 2019, **358**, 891–902.

32 Z. Qin, D. Zhao, L. Zhao, Q. Xiao, T. Wu, J. Zhang, C. Wan and G. Li, *Nanoscale Adv.*, 2019, **1**, 2529–2536.

33 Q. Shi, G. Ping, X. Wang, H. Xu, J. Li, J. Cui, H. Abroshan, H. Ding and G. Li, *J. Mater. Chem. A*, 2019, **7**, 2253–2260.

34 S. Zhang, X. Gong, Q. Shi, G. Ping, H. Xu, A. Waleed and G. Li, *ACS Omega*, 2020, **5**, 15942–15948.

35 J. Hu, W. Fan, W. Ye, C. Huang and X. Qiu, *Appl. Catal., B*, 2014, **158–159**, 182–189.

36 A. Sudhaik, P. Raizada, P. Shandilya, D.-Y. Jeong, J.-H. Lim and P. Singh, *J. Ind. Eng. Chem.*, 2018, **67**, 28–51.

37 S. O. Ganiyu, C. A. Martínez-Huitle and M. A. Rodrigo, *Appl. Catal., B*, 2020, **270**, 118857.

38 J. Li, H. Li, G. Zhan and L. Zhang, *Acc. Chem. Res.*, 2017, **50**, 112–121.

39 B. Li, S. Liu, C. Lai, G. Zeng, M. Zhang, M. Zhou, D. Huang, L. Qin, X. Liu, Z. Li, N. An, F. Xu, H. Yi, Y. Zhang and L. Chen, *Appl. Catal., B*, 2020, **266**, 118650.

40 L. Ye, X. Jin, C. Liu, C. Ding, H. Xie, K. H. Chu and P. K. Wong, *Appl. Catal., B*, 2016, **187**, 281–290.

41 J. Jiang, K. Zhao, X. Xiao and L. Zhang, *J. Am. Chem. Soc.*, 2012, **134**, 4473–4476.

42 Z. Fan, Y. Zhao, W. Zhai, L. Qiu, H. Li and M. R. Hoffmann, *RSC Adv.*, 2016, **6**, 2028–2031.

43 L. Wang, J. Shang, W. Hao, S. Jiang, S. Huang, T. Wang, Z. Sun, Y. Du, S. Dou, T. Xie, D. Wang and J. Wang, *Sci. Rep.*, 2014, **4**, 7384.

44 G. Zhang, L. Zhang, Y. Liu, L. Liu, C.-P. Huang, H. Liu and J. Li, *ACS Appl. Mater. Interfaces*, 2016, **8**, 26783–26793.

45 D. Mao, S. Ding, L. Meng, Y. Dai, C. Sun, S. Yang and H. He, *Appl. Catal., B*, 2017, **207**, 153–165.

46 Y. Huang, H. Li, W. Fan, F. Zhao, W. Qiu, H. Ji and Y. Tong, *ACS Appl. Mater. Interfaces*, 2016, **8**, 27859–27867.

47 Q. Mu, Q. Zhang, H. Wang and Y. Li, *J. Mater. Chem.*, 2012, **22**, 16851–16857.

48 Y. Wu, B. Yuan, M. Li, W.-H. Zhang, Y. Liu and C. Li, *Chem. Sci.*, 2015, **6**, 1873–1878.

49 Y. Shi, X. Xiong, S. Ding, X. Liu, Q. Jiang and J. Hu, *Appl. Catal., B*, 2018, **220**, 570–580.

50 H. Li, J. Shang, Z. Ai and L. Zhang, *J. Am. Chem. Soc.*, 2015, **137**, 6393–6399.

51 H. Cheng, B. Huang, P. Wang, Z. Wang, Z. Lou, J. Wang, X. Qin, X. Zhang and Y. Dai, *Chem. Commun.*, 2011, **47**, 7054–7056.

52 X. Zhang, X. Liu, C. Fan, Y. Wang, Y. Wang and Z. Liang, *Appl. Catal., B*, 2013, **132–133**, 332–341.

53 G. He, C. Xing, X. Xiao, R. Hu, X. Zuo and J. Nan, *Appl. Catal., B*, 2015, **170–171**, 1–9.

54 A. Waheed, Q. Shi, N. Maeda, D. M. Meier, Z. Qin, G. Li and A. Baiker, *Catalysts*, 2020, **10**, 933.

55 L. Armelao, G. Bottaro, C. Maccato and E. Tondello, *Dalton Trans.*, 2012, **41**, 5480–5485.

56 Z. Song, X. Dong, N. Wang, L. Zhu, Z. Luo, J. Fang and C. Xiong, *Chem. Eng. J.*, 2017, **317**, 925–934.

57 Z. Zhuang, Q. Peng and Y. Li, *Chem. Soc. Rev.*, 2011, **40**, 5492–5513.

58 M. Ikram, R. Tabassum, U. Qumar, S. Ali, A. Ul-Hamid, A. Haider, A. Raza, M. Imran and S. Ali, *RSC Adv.*, 2020, **10**, 20559–20571.

59 X. Gao, W. Peng, G. Tang, Q. Guo and Y. Luo, *J. Alloys Compd.*, 2018, **757**, 455–465.

60 W. Liu, Y. Shang, A. Zhu, P. Tan, Y. Liu, L. Qiao, D. Chu, X. Xiong and J. Pan, *J. Mater. Chem. A*, 2017, **5**, 12542–12549.

61 C. Ding, L. Ye, Q. Zhao, Z. Zhong, K. Liu, H. Xie, K. Bao, X. Zhang and Z. Huang, *J. CO2 Util.*, 2016, **14**, 135–142.

62 P. Cui, J. Wang, Z. Wang, J. Chen, X. Xing, L. Wang and R. Yu, *Nano Res.*, 2016, **9**, 593–601.

63 X. Yan, H. Zhao, T. Li, W. Zhang, Q. Liu, Y. Yuan, L. Huang, L. Yao, J. Yao, H. Su, Y. Su, J. Gu and D. Zhang, *Nanoscale*, 2019, **11**, 10203–10208.

64 C. Yu, W. Zhou, J. Yu, F. Cao and X. Li, *Chin. J. Chem.*, 2012, **30**, 721–726.

65 Y. Bai, T. Chen, P. Wang, L. Wang and L. Ye, *Chem. Eng. J.*, 2016, **304**, 454–460.

66 Y. Bai, L. Ye, T. Chen, P. Wang, L. Wang, X. Shi and P. K. Wong, *Appl. Catal., B*, 2017, **203**, 633–640.

67 S. Chu and A. Majumdar, *Nature*, 2012, **488**, 294–303.

68 C. Huang, Y. Wen, J. Ma, D. Dong, Y. Shen, S. Liu, H. Ma and Y. Zhang, *Nat. Commun.*, 2021, **12**, 320.

69 G. Zhou, Y. Shan, Y. Hu, X. Xu, L. Long, J. Zhang, J. Dai, J. Guo, J. Shen, S. Li, L. Liu and X. Wu, *Nat. Commun.*, 2018, **9**, 3366.

70 J. Kosco, M. Bidwell, H. Cha, T. Martin, C. T. Howells, M. Sachs, D. H. Anjum, S. Gonzalez Lopez, L. Zou, A. Wadsworth, W. Zhang, L. Zhang, J. Tellam, R. Sougrat, F. Laquai, D. M. DeLongchamp, J. R. Durrant and I. McCulloch, *Nat. Mater.*, 2020, **19**, 559–565.

71 M. Ikram, E. Umar, A. Raza, A. Haider, S. Naz, A. Ul-Hamid, J. Haider, I. Shahzadi, J. Hassan and S. Ali, *RSC Adv.*, 2020, **10**, 24215–24233.

72 A. Raza, U. Qumar, J. Hassan, M. Ikram, A. Ul-Hamid, J. Haider, M. Imran and S. Ali, *Appl. Nanosci.*, 2020, **10**, 3875–3899.

73 F. Deng, J.-P. Zou, L.-N. Zhao, G. Zhou, X.-B. Luo and S.-L. Luo, in *Nanomaterials for the Removal of Pollutants and Resource Reutilization*, ed. X. Luo and F. Deng, Elsevier, 2019, pp. 59–82, DOI: 10.1016/B978-0-12-814837-2.00003-2.

74 M. Z. Rahman and C. B. Mullins, *Acc. Chem. Res.*, 2019, **52**, 248–257.

75 M. Z. Rahman, M. G. Kibria and C. B. Mullins, *Chem. Soc. Rev.*, 2020, **49**, 1887–1931.

76 X. Chen, S. Shen, L. Guo and S. S. Mao, *Chem. Rev.*, 2010, **110**, 6503–6570.

77 D. Ravelli, D. Dondi, M. Fagnoni and A. Albini, *Chem. Soc. Rev.*, 2009, **38**, 1999–2011.

78 B. Ohtani, *J. Photochem. Photobiol., C*, 2010, **11**, 157–178.

79 M. Ikram, J. Hassan, M. Imran, J. Haider, A. Ul-Hamid, I. Shahzadi, M. Ikram, A. Raza, U. Qumar and S. Ali, *Appl. Nanosci.*, 2020, **10**, 3525–3528.

80 M. Ikram, J. Hassan, A. Raza, A. Haider, S. Naz, A. Ul-Hamid, J. Haider, I. Shahzadi, U. Qamar and S. Ali, *RSC Adv.*, 2020, **10**, 30007–30024.

81 T. Hisatomi, K. Takanabe and K. Domen, *Catal. Lett.*, 2015, **145**, 95–108.

82 Q. Usman, H. Jahanzeb, N. Sadia, H. Ali, R. Ali, U.-H. Anwar, H. Junaid, S. Iram, A. Iqbal and I. Muhammad, *Nanotechnology*, 2021, **32**, 255704.

83 J. E. Kroeze, T. J. Savenije and J. M. Warman, *J. Am. Chem. Soc.*, 2004, **126**, 7608–7618.

84 J. Bisquert, *Phys. Chem. Chem. Phys.*, 2008, **10**, 3175–3194.

85 M. Shen and M. A. Henderson, *J. Phys. Chem. Lett.*, 2011, **2**, 2707–2710.

86 J. Li, L. Cai, J. Shang, Y. Yu and L. Zhang, *Adv. Mater.*, 2016, **28**, 4059–4064.

87 S. Bai, X. Li, Q. Kong, R. Long, C. Wang, J. Jiang and Y. Xiong, *Adv. Mater.*, 2015, **27**, 3444–3452.

88 W. Wu, Z. Zhang, J. Di and W. Zhao, *ChemNanoMat*, 2019, **5**, 215–223.

89 S. Ning, X. Shi, H. Zhang, H. Lin, Z. Zhang, J. Long, Y. Li and X. Wang, *Sol. RRL*, 2019, **3**, 1900059.

90 M. Ji, R. Chen, J. Di, Y. Liu, K. Li, Z. Chen, J. Xia and H. Li, *J. Colloid Interface Sci.*, 2019, **533**, 612–620.

91 X. Xiong, T. Zhou, X. Liu, S. Ding and J. Hu, *J. Mater. Chem. A*, 2017, **5**, 15706–15713.

92 N. Du, H. B. Park, G. P. Robertson, M. M. Dal-Cin, T. Visser, L. Scoles and M. D. Guiver, *Nat. Mater.*, 2011, **10**, 372–375.

93 B. Kumar, M. Asadi, D. Pisasale, S. Sinha-Ray, B. A. Rosen, R. Haasch, J. Abiade, A. L. Yarin and A. Salehi-Khojin, *Nat. Commun.*, 2013, **4**, 2819.

94 H. Zhou, J. Guo, P. Li, T. Fan, D. Zhang and J. Ye, *Sci. Rep.*, 2013, **3**, 1667.

95 L. Wang, S.-q. Guo, Y. Chen, M. Pan, E. H. Ang and Z.-h. Yuan, *ChemPhotoChem*, 2020, **4**, 110–119.

96 J. Di, J. Xia, M. Ji, B. Wang, X. Li, Q. Zhang, Z. Chen and H. Li, *ACS Sustainable Chem. Eng.*, 2016, **4**, 136–146.

97 J. Liu, R. Li, X. Zu, X. Zhang, Y. Wang, Y. Wang and C. Fan, *Chem. Eng. J.*, 2019, **371**, 796–803.

98 Y. Bai, L. Ye, T. Chen, L. Wang, X. Shi, X. Zhang and D. Chen, *ACS Appl. Mater. Interfaces*, 2016, **8**, 27661–27668.

99 J. Di, J. Xia, M. F. Chisholm, J. Zhong, C. Chen, X. Cao, F. Dong, Z. Chi, H. Chen, Y.-X. Weng, J. Xiong, S.-Z. Yang, H. Li, Z. Liu and S. Dai, *Adv. Mater.*, 2019, **31**, 1807576.

100 T. Wang, C. Feng, J. Liu, D. Wang, H. Hu, J. Hu, Z. Chen and G. Xue, *Chem. Eng. J.*, 2021, **414**, 128827.

101 P. Qiu, J. Wang, Z. Liang, Y. Xue, Y. Zhou, X. Zhang, H. Cui, G. Cheng and J. Tian, *Chin. Chem. Lett.*, 2021, DOI: 10.1016/j.cclet.2021.03.077.

102 J. Wang, Y. Yu and L. Zhang, *Appl. Catal., B*, 2013, **136–137**, 112–121.

103 X. Xiao, C. Xing, G. He, X. Zuo, J. Nan and L. Wang, *Appl. Catal., B*, 2014, **148–149**, 154–163.

104 Y. Su, C. Ding, Y. Dang, H. Wang, L. Ye, X. Jin, H. Xie and C. Liu, *Appl. Surf. Sci.*, 2015, **346**, 311–316.

105 S. Sun, W. Wang, L. Zhang, L. Zhou, W. Yin and M. Shang, *Environ. Sci. Technol.*, 2009, **43**, 2005–2010.

106 J. Yang, L. Xu, C. Liu and T. Xie, *Appl. Surf. Sci.*, 2014, **319**, 265–271.

107 J. Xia, Y. Ge, J. Di, L. Xu, S. Yin, Z. Chen, P. Liu and H. Li, *J. Colloid Interface Sci.*, 2016, **473**, 112–119.

108 W. Zhang, X. Liu, X. a. Dong, F. Dong and Y. Zhang, *Chin. J. Catal.*, 2017, **38**, 2030–2038.

109 M. Ikram, M. I. Khan, A. Raza, M. Imran, A. Ul-Hamid and S. Ali, *Phys. E*, 2020, **124**, 114246.

110 M. Ji, J. Di, Y. Liu, R. Chen, K. Li, Z. Chen, J. Xia and H. Li, *Appl. Catal., B*, 2020, **268**, 118403.

111 X. Xiao, R. Hao, X. Zuo, J. Nan, L. Li and W. Zhang, *Chem. Eng. J.*, 2012, **209**, 293–300.

112 W. Zhang, X. a. Dong, B. Jia, J. Zhong, Y. Sun and F. Dong, *Appl. Surf. Sci.*, 2018, **430**, 571–577.

113 L. Ding, H. Chen, Q. Wang, T. Zhou, Q. Jiang, Y. Yuan, J. Li and J. Hu, *Chem. Commun.*, 2016, **52**, 994–997.

114 R. Yuan, S. Fan, H. Zhou, Z. Ding, S. Lin, Z. Li, Z. Zhang, C. Xu, L. Wu, X. Wang and X. Fu, *Angew. Chem., Int. Ed.*, 2013, **52**, 1035–1039.

115 H. Wang, S. Chen, D. Yong, X. Zhang, S. Li, W. Shao, X. Sun, B. Pan and Y. Xie, *J. Am. Chem. Soc.*, 2017, **139**, 4737–4742.

116 C. Huang, J. Hu, S. Cong, Z. Zhao and X. Qiu, *Appl. Catal., B*, 2015, **174–175**, 105–112.

117 J. Li, Y. Yu and L. Zhang, *Nanoscale*, 2014, **6**, 8473–8488.

118 G. Jiang, R. Wang, X. Wang, X. Xi, R. Hu, Y. Zhou, S. Wang, T. Wang and W. Chen, *ACS Appl. Mater. Interfaces*, 2012, **4**, 4440–4444.

119 J. Xia, L. Xu, J. Zhang, S. Yin, H. Li, H. Xu and J. Di, *CrystEngComm*, 2013, **15**, 10132–10141.

120 G. Jiang, X. Wang, Z. Wei, X. Li, X. Xi, R. Hu, B. Tang, R. Wang, S. Wang, T. Wang and W. Chen, *J. Mater. Chem. A*, 2013, **1**, 2406–2410.

121 M. Z. Shahid, R. Mehmood, M. Athar, J. Hussain, Y. Wei and A. Khaliq, *ACS Appl. Nano Mater.*, 2021, **4**, 746–758.

122 M. Gao, D. Zhang, X. Pu, H. Li, W. Li, X. Shao, D. Lv, B. Zhang and J. Dou, *Sep. Purif. Technol.*, 2016, **162**, 114–119.

123 J. Di, J. Xia, S. Yin, H. Xu, L. Xu, Y. Xu, M. He and H. Li, *RSC Adv.*, 2014, **4**, 14281–14290.

124 W. T. Li, W. Z. Huang, H. Zhou, H. Y. Yin, Y. F. Zheng and X. C. Song, *J. Alloys Compd.*, 2015, **638**, 148–154.

125 J. Zhou, J. Zhou, Z. Hu and L. Wang, *Mater. Sci. Semicond. Process.*, 2019, **90**, 112–119.

126 Z. Liu, B. Wu, Y. Zhao, J. Niu and Y. Zhu, *Ceram. Int.*, 2014, **40**, 5597–5603.

127 X. Tu, S. Qian, L. Chen and L. Qu, *J. Mater. Sci.*, 2015, **50**, 4312–4323.

128 B. Pare, B. Sarwan and S. B. Jonnalagadda, *Appl. Surf. Sci.*, 2011, **258**, 247–253.

129 W. Wang, R. Dai, L. Zhang, Q. Wu, X. Wang, S. Zhang, T. Shao, F. Zhang, J. Yan and W. Zhang, *J. Mater. Sci.*, 2020, **55**, 11226–11240.

130 W. Yang, Y. Wen, R. Chen, D. Zeng and B. Shan, *Phys. Chem. Chem. Phys.*, 2014, **16**, 21349–21355.

131 J. Xia, M. Ji, W. Li, J. Di, H. Xu, M. He, Q. Zhang and H. Li, *Colloids Surf., A*, 2016, **489**, 343–350.

132 W. Zhao, C. Li, A. Wang, C. Lv, W. Zhu, S. Dou, Q. Wang and Q. Zhong, *Phys. Chem. Chem. Phys.*, 2017, **19**, 28696–28709.

133 A. Dash, S. Sarkar, V. N. K. B. Adusumalli and V. Mahalingam, *Langmuir*, 2014, **30**, 1401–1409.

134 M. Arumugam and M. Y. Choi, *J. Ind. Eng. Chem.*, 2020, **81**, 237–268.

135 X. Chen, L. Liu and F. Huang, *Chem. Soc. Rev.*, 2015, **44**, 1861–1885.

136 G. Liu, C. Sun, L. Cheng, Y. Jin, H. Lu, L. Wang, S. C. Smith, G. Q. Lu and H.-M. Cheng, *J. Phys. Chem. C*, 2009, **113**, 12317–12324.

137 J. Li, K. Zhao, Y. Yu and L. Zhang, *Adv. Funct. Mater.*, 2015, **25**, 2189–2201.

138 X. Zhang and L. Zhang, *J. Phys. Chem. C*, 2010, **114**, 18198–18206.

139 L. Zeng, F. Zhe, Y. Wang, Q. Zhang, X. Zhao, X. Hu, Y. Wu and Y. He, *J. Colloid Interface Sci.*, 2019, **539**, 563–574.

140 H. Li, J. Shang, H. Zhu, Z. Yang, Z. Ai and L. Zhang, *ACS Catal.*, 2016, **6**, 8276–8285.

141 H. Li, J. Li, Z. Ai, F. Jia and L. Zhang, *Angew. Chem., Int. Ed.*, 2018, **57**, 122–138.

142 M. Guan, C. Xiao, J. Zhang, S. Fan, R. An, Q. Cheng, J. Xie, M. Zhou, B. Ye and Y. Xie, *J. Am. Chem. Soc.*, 2013, **135**, 10411–10417.

143 D. Cui, L. Wang, K. Xu, L. Ren, L. Wang, Y. Yu, Y. Du and W. Hao, *J. Mater. Chem. A*, 2018, **6**, 2193–2199.

144 B. Gao, J.-R. Zhang, L. Chen, J. Guo, S. Shen, C.-T. Au, S.-F. Yin and M.-Q. Cai, *Appl. Surf. Sci.*, 2019, **492**, 157–165.

145 J. Cao, B. Xu, H. Lin, B. Luo and S. Chen, *Chem. Eng. J.*, 2012, **185–186**, 91–99.

146 X. Jia, J. Cao, H. Lin, M. Zhang, X. Guo and S. Chen, *Appl. Catal., B*, 2017, **204**, 505–514.

147 Y. Wang, Y. Long, Z. Yang and D. Zhang, *J. Hazard. Mater.*, 2018, **351**, 11–19.

148 M. Sun, Q. Wei, Y. Shao, B. Du, T. Yan, L. Yan and D. Li, *Appl. Catal., B*, 2018, **233**, 250–259.

149 Y. Xu, Y. You, H. Huang, Y. Guo and Y. Zhang, *J. Hazard. Mater.*, 2020, **381**, 121159.

150 X. Yan, Z. Wu, P. Yang, Y. Mao, B. Liu, Y. Zhao, H. Shen and D. Wang, *Catal. Commun.*, 2019, **123**, 91–95.

151 H. Peng, L. Wang, J. Xu, S. Jiang, X. Xu and Q. Zhang, *Mater. Lett.*, 2019, **256**, 126694.

152 J. Xu, Y.-G. Mao, T. Liu and Y. Peng, *CrystEngComm*, 2018, **20**, 2292–2298.

153 D. Hou, F. Tang, B. Ma, M. Deng, X.-q. Qiao, Y.-L. Liu and D.-S. Li, *CrystEngComm*, 2019, **21**, 4158–4168.

154 Y. Peng, P.-P. Yu, Q.-G. Chen, H.-Y. Zhou and A.-W. Xu, *J. Phys. Chem. C*, 2015, **119**, 13032–13040.

155 J. Jiang, X. Zhang, P. Sun and L. Zhang, *J. Phys. Chem. C*, 2011, **115**, 20555–20564.

156 X. Zhang, L. Zhang, T. Xie and D. Wang, *J. Phys. Chem. C*, 2009, **113**, 7371–7378.

157 Q. Xiang, J. Yu and M. Jaroniec, *Chem. Soc. Rev.*, 2012, **41**, 782–796.

158 W. Tu, Y. Zhou, Q. Liu, S. Yan, S. Bao, X. Wang, M. Xiao and Z. Zou, *Adv. Funct. Mater.*, 2013, **23**, 1743–1749.

159 F. Gao, D. Zeng, Q. Huang, S. Tian and C. Xie, *Phys. Chem. Chem. Phys.*, 2012, **14**, 10572–10578.

160 H. Liu, Y. Su, Z. Chen, Z. Jin and Y. Wang, *J. Hazard. Mater.*, 2014, **266**, 75–83.

161 H. Feng, Z. Xu, L. Wang, Y. Yu, D. Mitchell, D. Cui, X. Xu, J. Shi, T. Sannomiya, Y. Du, W. Hao and S. X. Dou, *ACS Appl. Mater. Interfaces*, 2015, **7**, 27592–27596.

162 J. Feng, X. Qian, C.-W. Huang and J. Li, *Nat. Photonics*, 2012, **6**, 866–872.

163 L. Wang, L. Wang, Y. Du, X. Xu and S. X. Dou, *Mater. Today Phys.*, 2021, **16**, 100294.

164 D. Shiri, Y. Kong, A. Buin and M. P. Anantram, *Appl. Phys. Lett.*, 2008, **93**, 073114.

165 R. Li, F. Zhang, D. Wang, J. Yang, M. Li, J. Zhu, X. Zhou, H. Han and C. Li, *Nat. Commun.*, 2013, **4**, 1432.

166 L. Ye, X. Liu, Q. Zhao, H. Xie and L. Zan, *J. Mater. Chem. A*, 2013, **1**, 8978–8983.

167 J. Shang, W. Hao, X. Lv, T. Wang, X. Wang, Y. Du, S. Dou, T. Xie, D. Wang and J. Wang, *ACS Catal.*, 2014, **4**, 954–961.

168 K. Maeda, K. Teramura, D. Lu, T. Takata, N. Saito, Y. Inoue and K. Domen, *Nature*, 2006, **440**, 295.

169 Y. Liu, W.-J. Son, J. Lu, B. Huang, Y. Dai and M.-H. Whangbo, *Chem.–Eur. J.*, 2011, **17**, 9342–9349.

170 K. Ren, J. Liu, J. Liang, K. Zhang, X. Zheng, H. Luo, Y. Huang, P. Liu and X. Yu, *Dalton Trans.*, 2013, **42**, 9706–9712.

171 Z. Liu, J. Niu, P. Feng and Y. Zhu, *Ceram. Int.*, 2015, **41**, 4608–4615.

172 H. Cheng, B. Huang and Y. Dai, *Nanoscale*, 2014, **6**, 2009–2026.

173 Y. Yang, C. Zhang, C. Lai, G. Zeng, D. Huang, M. Cheng, J. Wang, F. Chen, C. Zhou and W. Xiong, *Adv. Colloid Interface Sci.*, 2018, **254**, 76–93.

174 Z. Wang, M. Chen, D. Huang, G. Zeng, P. Xu, C. Zhou, C. Lai, H. Wang, M. Cheng and W. Wang, *Chem. Eng. J.*, 2019, **374**, 1025–1045.

175 H. Cheng, B. Huang, Y. Dai, X. Qin and X. Zhang, *Langmuir*, 2010, **26**, 6618–6624.

176 C. Xue, J. Xia, T. Wang, S. Zhao, G. Yang, B. Yang, Y. Dai and G. Yang, *Mater. Lett.*, 2014, **133**, 274–277.

177 Y. Geng, N. Li, J. Ma and Z. Sun, *J. Energy Chem.*, 2017, **26**, 416–421.

178 M. Rashid, M. Ikram, A. Haider, S. Naz, J. Haider, A. Ul-Hamid, A. Shahzadi and M. Aqeel, *Dalton Trans.*, 2020, **49**, 8314–8330.

179 M. Ali, S. Sharif, S. Anjum, M. Imran, M. Ikram, M. Naz and S. Ali, *Mater. Res. Express*, 2020, **6**, 1250–1255.

180 J. Liu, Z. Luo, W. Han, Y. Zhao and P. Li, *Mater. Sci. Semicond. Process.*, 2020, **106**, 104761.

181 L. Wang, Z. Li, J. Chen, Y. Huang, H. Zhang and H. Qiu, *Environ. Pollut.*, 2019, **249**, 801–811.

182 L. Zhu, H. Li, P. Xia, Z. Liu and D. Xiong, *ACS Appl. Mater. Interfaces*, 2018, **10**, 39679–39687.

183 L. Zhu, H. Li, Z. Liu, P. Xia, Y. Xie and D. Xiong, *J. Phys. Chem. C*, 2018, **122**, 9531–9539.

184 M. Laurenti, N. Garino, G. Canavese, S. Hernandéz and V. Cauda, *ACS Appl. Mater. Interfaces*, 2020, **12**, 25798–25808.

185 Y. Chen, Y. Wang, J. Fang, B. Dai, J. Kou, C. Lu and Y. Zhao, *Chin. J. Catal.*, 2021, **42**, 184–192.

186 R. Beura, R. Pachaiappan and T. Paramasivam, *J. Phys. Chem. Solids*, 2021, **148**, 109689.

187 H. J. Biswal, A. Yadav, P. R. Vundavilli and A. Gupta, *RSC Adv.*, 2021, **11**, 1623–1634.

188 O. Yanushevska, T. Dontsova, S. Nahirniak and V. Alisova, TiO$_2$–ZnO Nanocomposites for Photodegradation of Dyes in Water Bodies, in *Nanomaterials and Nanocomposites, Nanostructure Surfaces, and Their Applications*, ed. O. Fesenko and L. Yatsenko, Springer International Publishing, Cham, 2021, pp. 719–731.

189 L. Zhou, Z. Han, G.-D. Li and Z. Zhao, *J. Phys. Chem. Solids*, 2021, **148**, 109719.

190 A. H. Zyoud, M. Dwikat, S. Anabtawi, R. Alkowni, N. Qamhieh, A. Hajamohideen, S. H. Zyoud, M. H. S. Helal, S. H. Zyoud, H. Nassar and H. S. Hilal, *JOM*, 2021, **73**, 420–431.

191 S. Sharon Tamil Selvi, G. Hannah Priya, R. Ragu, D. Ancelia, L. Allwin Joseph and J. Mary Linet, *J. Cluster Sci.*, 2021, DOI: 10.1007/s10876-020-01963-9.

192 H. J. Yoon, Y. I. Choi, E.-S. Jang and Y. Sohn, *J. Ind. Eng. Chem.*, 2015, **32**, 137–152.

193 Z. Zhang, C. Shao, X. Li, L. Zhang, H. Xue, C. Wang and Y. Liu, *J. Phys. Chem. C*, 2010, **114**, 7920–7925.

194 L. Kong, Z. Jiang, T. Xiao, L. Lu, M. O. Jones and P. P. Edwards, *Chem. Commun.*, 2011, **47**, 5512–5514.

195 M. M. Khan, S. F. Adil and A. Al-Mayouf, *J. Saudi Chem. Soc.*, 2015, **19**, 462–464.

196 Q. W. Cao, X. Cui, Y. F. Zheng and X. C. Song, *J. Alloys Compd.*, 2016, **670**, 12–17.

197 Y. Zhao, R. Li, L. Mu and C. Li, *Cryst. Growth Des.*, 2017, **17**, 2923–2928.

198 G. Huang and Y. Zhu, *Mater. Sci. Eng., B*, 2007, **139**, 201–208.

199 X. Ma, Z. Ma, T. Liao, X. Liu, Y. Zhang, L. Li, W. Li and B. Hou, *J. Alloys Compd.*, 2017, **702**, 68–74.

200 M. Su, C. He, L. Zhu, Z. Sun, C. Shan, Q. Zhang, D. Shu, R. Qiu and Y. Xiong, *J. Hazard. Mater.*, 2012, **229–230**, 72–82.

201 Z. Li, Y. Qu, K. Hu, M. Humayun, S. Chen and L. Jing, *Appl. Catal., B*, 2017, **203**, 355–362.

202 C. Liu, X. Dong, Y. Hao, X. Wang, H. Ma and X. Zhang, *RSC Adv.*, 2017, **7**, 22415–22423.

203 W. Liu, J. Cai and Z. Li, *ACS Sustainable Chem. Eng.*, 2015, **3**, 277–282.

204 X. Tu, S. Luo, G. Chen and J. Li, *Chem.–Eur. J.*, 2012, **18**, 14359–14366.

205 M. J. Kale, T. Avanesian and P. Christopher, *ACS Catal.*, 2014, **4**, 116–128.

206 Z. Zhang, Y. Zhou, S. Yu, M. Chen and F. Wang, *Mater. Lett.*, 2015, **150**, 97–100.

207 H.-x. Pan, L.-p. Feng, W. Zeng, Q.-c. Zhang, X.-d. Zhang and Z.-t. Liu, *Inorg. Chem.*, 2019, **58**, 13195–13202.

208 Z. Jiang, Y. Liu, T. Jing, B. Huang, Z. Wang, X. Zhang, X. Qin and Y. Dai, *RSC Adv.*, 2015, **5**, 47261–47264.

209 J. Li, L. Cai, J. Shang, Y. Yu and L. Zhang, *Adv. Mater.*, 2016, **28**, 4059–4064.

210 S. Ning, X. Shi, H. Zhang, H. Lin, Z. Zhang, J. Long, Y. Li and X. Wang, *Sol. RRL*, 2019, **3**, 1900059.

211 Z. Ma, P. Li, L. Ye, Y. Zhou, F. Su, C. Ding, H. Xie, Y. Bai and P. K. Wong, *J. Mater. Chem. A*, 2017, **5**, 24995–25004.

212 L. Liang, F. Lei, S. Gao, Y. Sun, X. Jiao, J. Wu, S. Qamar and Y. Xie, *Angew. Chem., Int. Ed.*, 2015, **54**, 13971–13974.

213 L. Ye, H. Wang, X. Jin, Y. Su, D. Wang, H. Xie, X. Liu and X. Liu, *Sol. Energy Mater. Sol. Cells*, 2016, **144**, 732–739.

214 L. Ye, X. Jin, X. Ji, C. Liu, Y. Su, H. Xie and C. Liu, *Chem. Eng. J.*, 2016, **291**, 39–46.

215 F. Chen, H. Huang, L. Ye, T. Zhang, Y. Zhang, X. Han and T. Ma, *Adv. Funct. Mater.*, 2018, **28**, 1804284.

216 Y. Zhou, Z. Tian, Z. Zhao, Q. Liu, J. Kou, X. Chen, J. Gao, S. Yan and Z. Zou, *ACS Appl. Mater. Interfaces*, 2011, **3**, 3594–3601.

217 S. Wang, X. Hai, X. Ding, K. Chang, Y. Xiang, X. Meng, Z. Yang, H. Chen and J. Ye, *Adv. Mater.*, 2017, **29**, 1701774.

218 P. Li, Z. Zhou, Q. Wang, M. Guo, S. Chen, J. Low, R. Long, W. Liu, P. Ding, Y. Wu and Y. Xiong, *J. Am. Chem. Soc.*, 2020, **142**, 12430–12439.